

The Nature of Weak MgII Absorbing Structures^{1,2}

Nikola Milutinović³, Jane R. Rigby⁴, Joseph R. Masiero^{3,5}, Ryan S. Lynch³, Chris Palma³,
and Jane C. Charlton³

ABSTRACT

We consider geometries and possible physical models for weak low ionization absorbers based on the relative incidence of low and high ionization absorption systems. To facilitate this, we present a survey of weak low ionization absorption systems ($W_r(2796) \leq 0.3\text{\AA}$) in 35 quasar spectra from the archive of high resolution, ultra-violet *HST*/STIS data. When possible, we supplemented these spectra with Keck/HIRES and *HST*/FOS data that cover more transitions over a larger range of wavelengths. We found a total of 16 metal-line systems, with low and/or high ionization absorption detected. It is known that the weak low ionization absorbers (which we probe with MgII $\lambda\lambda 2796, 2803$ or through the combination of CII $\lambda 1335$ and SiII $\lambda 1260$) trace an abundant population of metal-enriched regions (close to solar metallicity). Generally, models show that these systems have a $\sim 10\text{pc}$ region of higher density gas and a $\sim 1\text{kpc}$ region that represents a lower density phase of higher ionization absorption. The goal of our survey was to compare absorption systems detected in low and/or high ionization gas (the latter traced with CIV $\lambda\lambda 1548, 1550$ absorption). We find the following: 1. All but 1 of the 10 weak low ionization systems have a related high ionization phase. In 3 cases the high ionization gas has only a single component, kinematically centered on the low ionization absorption, and in the other 6 cases there are

¹Based in part on observations obtained with the NASA/ESA *Hubble Space Telescope*, which is operated by the STScI for the Association of Universities for Research in Astronomy, Inc., under NASA contract NAS5-26555.

²Based in part on observations obtained at the W. M. Keck Observatory, which is operated as a scientific partnership among Caltech, the University of California, and NASA. The Observatory was made possible by the generous financial support of the W. M. Keck Foundation.

³Department of Astronomy and Astrophysics, The Pennsylvania State University, University Park, PA 16802, *milni, charlton, cpalma@astro.psu.edu*

⁴Department of Astronomy, University of Arizona, Tucson, AZ, 85721, *jr Rigby@as.arizona.edu*

⁵Institute for Astronomy, University of Hawaii, 2680 Woodlawn Drive, Honolulu, HI 96822, *masiero@ifa.hawaii.edu*

additional high ionization components offset in velocity. There is one system, toward quasar 3C 273, without a high ionization cloud; 2. There are just 6 systems with only a high ionization phase as compared to the 9 systems with both low and high ionization phases; 3. The high ionization absorption in weak low ionization systems is, on average, stronger than in systems with only high ionization absorption; 4. The high ionization absorption in weak low ionization systems has similar kinematic structure to that in high ionization only systems. We find that filamentary and sheetlike geometries are favored, due to the relatively small observed cross-section of high ionization only systems. Our statistical arguments suggest that, although low ionization absorbers are not closely associated with luminous galaxies, they arise in their immediate environments within the cosmic web.

Subject headings: intergalactic medium — quasars: absorption lines

1. Introduction

Quasar absorption line spectroscopy is a powerful probe for the investigation of gas in the cosmic web. It offers a high sensitivity that makes it possible to trace different gas phases over a large range of redshifts, exploring both the intergalactic medium and a variety of morphologies and evolutionary stages of galaxies.

The MgII resonant doublet has been extensively used to trace metals in galaxies at $0.3 < z < 2.2$, the redshift range for which MgII lies in the optical. It is found that these low ionization systems, with $W_r(2796) \geq 0.3 \text{ \AA}$, produce Lyman limit breaks (Churchill et al. 2000). The gas kinematics, evident in high resolution absorption profiles, are consistent with material in both the disks and extended halos of the host galaxies (Charlton & Churchill 1998; Steidel et al. 2002). Almost all of these “strong” MgII systems are found within $38h^{-1}$ kpc of $> 0.05L_K^*$ galaxies (Bergeron & Boissé 1991; Bergeron et al. 1992; Le Brun et al. 1993; Steidel, Dickinson, & Persson 1994; Steidel 1995; Steidel et al. 1997). Furthermore, both observationally and theoretically, it is also expected that metal-rich absorbing gas can be found out to distances of at least $100h^{-1}$ kpc from luminous galaxies (Chen, Lanzetta, & Webb 2001; Ćirković, Samurović, & Djorić 2000). This gas can be detected through absorption in higher ionization species and/or as weak low ionization absorption.

Weak low ionization absorbers, with $0.02 \leq W_r(2796) \leq 0.3 \text{ \AA}$, constitute a significant fraction of the high HI column density regime ($15.8 < \log N(\text{HI}) < 16.8 \text{ cm}^{-2}$) of the Ly α forest at $z \sim 1$ (Rigby et al. 2002). With $dN/dz = 1.74 \pm 0.10$ for $0.4 < z < 1.4$,

they are twice as likely to be found along the quasar line of sight as strong low ionization absorbers (Churchill et al. 1999). The majority of these systems arise in an optically thin, sub-Lyman limit environment (Churchill et al. 2000). Unlike strong absorbers, weak low ionization absorbers typically are not associated with bright galaxies (with $L \geq 0.05L_*$) to within a $50h^{-1}$ kpc impact parameter of the quasar line of sight (Churchill et al. (1999); but see Churchill et al. (2005) for exceptions). This suggests that weak low ionization systems are a physically different population from strong absorbers, a result confirmed by the MgII equivalent width distribution measured from the Sloan Digital Sky Survey (Nestor, Turnshek, & Rao 2005).

Two thirds of weak low ionization absorbers have only a single narrow component with a Doppler b parameter of just a few km s^{-1} (Churchill et al. 1999; Rigby et al. 2002). Detection of FeII in some of these systems indicates a small ionization parameter and high density, which implies a small size, < 10 pc (Rigby et al. 2002). Based on photoionization models, at least some single-cloud weak low ionization absorbers without detected FeII are constrained to have similarly small sizes (Charlton et al. 2003). The absence of a Lyman limit break and the strength of the Lyman series lines provide constraints on the absorbers’ metallicities. Surprisingly, the derived metallicities are almost always greater than 10% solar, and are often as high as the solar value (Rigby et al. 2002; Charlton et al. 2003). Those absorbers with a large iron to magnesium ratio must incorporate material from Type Ia supernovae, in which case the metals would be generated “in-situ”. Their large observed numbers along quasar lines of sight, in combination with the small derived sizes, suggests that single-cloud low ionization systems must be extremely abundant. If they are assumed to have a spherical geometry there would be over a million such structures per bright galaxy. Most of the single-cloud weak low ionization absorbers have an associated higher ionization phase ¹ that gives rise to CIV absorption (Rigby et al. 2002). Photoionization modeling of three systems along the PG 1634 + 706 line of sight showed that low ionization absorption arises in a relatively high density region ($\sim 0.01 \text{ cm}^{-3}$) with a thickness of 0.1–100 pc. Higher ionization absorption arises in one or more lower density regions ($\sim 10^{-3} \text{ cm}^{-3}$), with sizes on the order of a kiloparsec (Charlton et al. 2003).

The other third of the weak low ionization absorbers have multiple, rather than single, low ionization clouds. Modeling of one of these systems, toward PG 1634+704 led to a derived, low metallicity of $\sim 3\%$ solar in the low ionization gas (Zonak et al. 2004). The kinematics of the low and high ionization gas suggested an origin in a pair of dwarf galaxies or in a symmetric wind from a starbursting dwarf (Zonak et al. 2004). Also, Rosenberg

¹A physically distinct region (or regions) that has a different density and/or temperature.

et al. (2003) have suggested that local analogs to weak low ionization absorbers are related to winds from starbursting dwarfs. In the case of the weak low ionization absorber at $z = 0.0052$ toward 3C 273 (Tripp et al. 2002), there is a post–starbursting dwarf galaxy, with a consistent redshift, at an impact parameter of $50h^{-1}$ kpc (Stocke et al. 2004). If winds from dwarfs typically produce multiple-cloud, weak low ionization absorption, then dwarf galaxies could be responsible for a large fraction of that absorber population. On the other hand, there is evidence that some multiple-cloud weak low ionization absorbers are produced by lines of sight through the outskirts of luminous galaxies (Masiero et al. 2005; Ding et al. 2005). This subclass would simply be an extension of the strong low ionization absorber population, which is directly produced by luminous galaxies (Ding et al. 2005).

The single-cloud weak low ionization absorbers present a dilemma. They are not closely related to luminous galaxies like strong absorbers, yet they have high metallicities inconsistent with production in the traditional gas phase of dwarfs. Rigby et al. (2002) suggested that they might be produced in Population III, pre-galactic star clusters or in supernovae remnants in very low luminosity galaxies, but these are only examples from possible classes of scenarios. In this paper, we seek constraints on the nature of the physical structures that produce the low and high ionization phase absorption in single–cloud, weak low ionization absorption line systems.

Our strategy is to compare the relative numbers and kinematics of systems with detected absorption from both low and high ionization phases to those of systems without absorption detected from one or the other of those phases. For example, in principle, the low ionization absorption could be produced in a small spherical region embedded in a much larger spherical structure that produces CIV absorption. In this case, we would expect that most systems have only high ionization absorption. We use the archive of *Hubble Space Telescope* (HST)/ Space Telescope Imaging Spectrograph (STIS) Echelle spectra ($R = 30,000$ or $45,000$) (Kimble et al. 1998) in order to make these comparisons, considering systems with coverage of CIV and at least some low ionization transitions (SiII λ 1260, CII λ 1335, and/or MgII $\lambda\lambda$ 2796, 2803).

In § 2, we briefly describe the characteristics of our sample, and the search method. In § 3 we describe the specific systems that we found. In § 4, we present statistical results and Voigt profile fits. In the discussion of the paper, § 5 and § 6, we apply our results to simple thought experiments in order to constrain possible geometries of the systems, and finally to connect these models to physical interpretations.

2. Data and Method

To facilitate our study, we searched for absorption systems at $0 < z < 1$ for which high resolution coverage of both low and high ionization transitions is available. The *HST*/STIS (Kimble et al. 1998) Echelle archive provides an excellent database for this study. When possible, we supplemented these data with Keck I/High Resolution Spectrograph (HIRES) (Vogt et al. 1994) spectra in order to obtain coverage of MgII and FeII. For a few systems, the high resolution data were supplemented by data obtained with the *HST*/Faint Object Spectrograph (FOS), which provided additional wavelength coverage at lower resolution.

2.1. STIS Archive

We searched 35 Echelle spectra of quasars from the *HST*/STIS archive that were available before May 2004 (Tables 1 and 2). These represented almost all of the available Echelle datasets. We eliminated several spectra due to poor S/N (< 5 per pixel), since these are not suitable for a study of weak low ionization absorption. All the spectra were obtained with the medium resolution gratings, E140M, with $R = 45,800$, and E230M, with $R = 30,000$. These resolutions correspond to 6.5 km s^{-1} and 10 km s^{-1} , respectively. $S/N = 5$ corresponds to an observed equivalent width limit between ~ 0.02 and 0.03 \AA in the E140M spectra, and between ~ 0.06 and 0.1 \AA in the E230M spectra. For data reduction, we used the standard STIS pipeline (Brown et al. 2002). Separate exposures and overlapping orders were combined using standard procedures described in Narayanan et al. (2005).

2.2. Keck/HIRES

Since *HST*/STIS does not cover of MgII $\lambda\lambda 2796, 2803$ for the observed redshift interval, we supplement the *HST*/STIS data with Keck I/HIRES data for PG 1634 + 706, PG 1206 + 459, PG 1248 + 401, PG 1241 + 176, PG 0117 + 210, CSO 873, and PG 0454 – 220 (Churchill et al. 1999; Churchill & Vogt 2001). For many systems for which MgII was not covered, SiII λ 1260 and CII λ 1335 were used to represent the strength of low ionization absorption. Since MgII is the most common tracer of low ionization systems at $z > 0.4$, for calibration purposes we used the Keck/HIRES dataset in conjunction with *HST*/STIS to find systems with all three transitions, SiII, CII, and MgII, detected (see § 2.4).

The optical spectra were obtained with the HIRES spectrograph (Vogt et al. 1994) on the Keck I telescope. The resolution is $R = 45,000$, corresponding to 6.6 km s^{-1} . These spectra have signal to noise ratios ranging from 15 to 30 (per pixel) in the continuum near

Mg II.

2.3. FOS

The *HST*/FOS data provided wavelength coverage of the Ly α transition for the few systems for which this transition was not covered by higher resolution *HST*/STIS observations. The *HST*/FOS spectra were obtained with the G130 or G190 gratings, which had resolution $R = 1,300$, corresponding to $\sim 230 \text{ km s}^{-1}$.

2.4. Search Method

The goal of our survey was to detect systems at $0 < z < 1$ which have high resolution wavelength coverage of both C IV and representative low ionization transitions (Mg II $\lambda\lambda 2796, 2803$, and/or Si II $\lambda 1260$ and C II $\lambda 1335$).

We first searched for the C IV $\lambda\lambda 1548, 1550$ doublet in the 35 quasar spectra from the STIS/Echelle archive. We compiled a list of 5σ detections using the method described in Schneider et al. (1993). We assumed each detection to be a candidate for the C IV $\lambda 1548$ line, the stronger transition of the C IV doublet. Then we searched for absorption at the corresponding C IV $\lambda 1550$ line position. A doublet candidate was designated if the significance of the detection at that position was $> 3 \sigma$, scaled down from 5σ by the expected C IV doublet ratio. For each of the doublet candidates we searched the *HST*/STIS spectrum for the Ly α transition at the same redshift. Detection of Ly α absorption over the full velocity range of the C IV detection was one criterion used to assess the reality of the doublet. If Ly α was not covered by the *HST*/STIS spectrum, we considered whether it was detected in any available spectra from *HST*/FOS. For each doublet candidate, we also visually inspected the alignment and the profile shapes of the doublet lines. If the lines closely correspond to one another, and there is no contradictory indication from Ly α , we consider the system to be “real”. In order to be included in our sample we also required that the S/N and coverage of available spectra allowed for detection of low ionization absorption tracers.

We measured the equivalent widths or equivalent width limits at the expected positions of the low ionization features in all of the “real” systems. For some systems, Mg II $\lambda\lambda 2796, 2803$ was covered in our Keck/HIRES data. However, when those data were not available, since Mg II $\lambda\lambda 2796, 2803$ is not covered in the *HST*/STIS spectra for absorbers at $z > 0.1$, we used the Si II $\lambda 1260$ and C II $\lambda 1335$ transitions as tracers of the low ionization phase. We formed a calibration sample, including all systems for which we have coverage of Mg II $\lambda\lambda 2796, 2803$

and either C II λ 1335 or Si II λ 1260. To our survey systems, we added five additional systems that failed to satisfy our survey requirements (e.g., have no coverage of C IV), but have the necessary coverage for this calibration. These additional systems are found toward PG 0117+210 at $z = 0.7290$, 1.3250 , and 1.3430 , toward PG 1206+459 at $z = 0.9343$, and toward PG1634+706 at $z = 1.0400$.

The equivalent widths of Mg II λ 2796, Si II λ 1260, and C II λ 1335 for a given system are highly correlated. The probability that the distribution of Mg II λ 2796 relative to Si II λ 1260 is drawn from a random distribution is only 0.17% by the Student’s t-Test, with a correlation coefficient of 0.88. Similarly, Mg II λ 2796 is closely correlated with C II λ 1335, with a correlation coefficient of 0.87, and with only a 0.21% chance of being drawn from a random distribution. The mean ratio $W_r(\text{C II } \lambda 1335)/W_r(\text{Mg II } \lambda 2796) = 1.07 \pm 0.49$ for the 9 relevant systems in our calibration sample. Similarly, the ratio, $W_r(\text{Si II } \lambda 1260)/W_r(\text{Mg II } \lambda 2796) = 0.52 \pm 0.20$, determined from the same number of systems.

Previous surveys for weak Mg II absorption (Churchill et al. 1999; Narayanan et al. 2005) applied a 5σ rest frame equivalent width detection threshold of 0.02\AA . Thus if we are sensitive to Si II λ 1260 to a 3σ limit of $W_r(1260) \gtrsim 0.01\text{\AA}$ and to C II λ 1335 to a 3σ limit of $W_r(1335) \gtrsim 0.02\text{\AA}$, according to the mean ratios above. Most of the relevant spectral coverage allows for detection of features significantly weaker than these limits, therefore, even with the observed variation in these ratios, we are sensitive to all systems equivalent to weak Mg II absorbers. Thus we can obtain an accurate indication of the fraction of systems with detected C IV that are equivalent to weak Mg II absorbers.

We also searched for systems which could be detected through low ionization absorption, but for which C IV absorption was not detected. We again used Si II λ 1260 and C II λ 1335 as tracers of weak Mg II systems, as in Narayanan et al. (2005).

3. Systems

We found 9 systems with both high and low ionization transitions detected, 6 systems with high ionization only, and 1 with low ionization only. We note that, as described in § 2.4, the detection limits for low ionization transitions associated with the 6 high ionization only systems were well below the traditional 0.02\AA detection limit for weak Mg II absorbers (Churchill et al. 1999; Narayanan et al. 2005). For convenient reference, in the headings for each system we give a simple classification. “SC” and “MC” denote single and multiple-cloud systems, respectively. The words “low” and “high” refer to the low (Si II, C II, and Mg II) and high ionization (C IV) transitions. If the word “low” or “high” is omitted, that means

that these transitions were covered, but were not detected in that system.

3.1. System Information

3.1.1. System 1 – 3c273, $z_{sys} = 0.0052$, SC low

This system, presented in Figure 1, is a single-cloud weak absorber, with only low ionization absorption detected. The low ionization absorption is detected as a single component in both Si II $\lambda 1260$ and C II $\lambda 1335$. The normalized Si III $\lambda 1207$ profile was produced by “fitting out” Galactic Ly α . C IV $\lambda \lambda 1548, 1550$ is not detected to a 3σ limit of $W_r(1548) < 0.0034 \text{ \AA}$. The Ly α , which was superimposed on Galactic Ly α , is centered on the low ionization absorption. For convenience of display, we divided by a model for the Galactic absorption in order to show the shape of the Ly α profile for this system. This system was reported by Tripp et al. (2002), and later discussed by Stocke et al. (2004) who reported a post-starburst galaxy at an impact parameter of $50h^{-1} \text{ kpc}$.

3.1.2. System 2 – RXJ 1230.8+0115, $z_{sys} = 0.0057$, MC low + SC high

This system, presented in Figure 2, is a multiple-cloud weak low ionization absorber, detected in Si II and C II. There are two components apparent in both Si II $\lambda 1260$ and C II $\lambda 1335$, which are also detected in Si IV $\lambda 1393$ and Si IV $\lambda 1402$. The region in which Si III $\lambda 1207$ would be observed is badly blended with Galactic Ly α . C IV $\lambda 1548$ is detected in the stronger, redward component, but not in the blueward component for which we derive a limit $W_r(1548) < 0.02 \text{ \AA}$. The Ly α line is strong and roughly centered on the two components. This system was published previously and discussed by Rosenberg et al. (2003), who also published FUSE data covering the Lyman series lines.

3.1.3. System 3 – PG 1211+143, $z_{sys} = 0.0512$, SC low + MC high

This system is a single-cloud weak low ionization absorber with multiple-component high ionization absorption. It is shown in Figure 3. Low ionization absorption is detected in Si II and C II. The blueward portion of the C II $\lambda 1335$ profile is blended with Galactic Si IV $\lambda \lambda 1393, 1402$. The C IV profile has three components, with the strongest centered on the single-cloud low ionization feature. The Si IV doublet lines show two components. The stronger one is centered on the low ionization absorption, and the weaker, blueward

component is centered on the coincident C IV cloud. Si III λ 1207 is detected, but it is blended with a Ly α line at $z = 0.0435$. The broad Ly α line is asymmetric relative to both the low and high ionization absorption, extending further to the red. This system was discussed by Stocke et al. (2004).

3.1.4. System 4 – PHL 1811, $z_{sys} = 0.0809$, SC low + SC high

This system, presented in Figure 4, is a single-cloud weak low ionization system, with a single component high ionization profile. Low ionization absorption is detected in Si II λ 1190, Si II λ 1193, Si II λ 1260, and Si II λ 1527, as well as in C II λ 1335. The blueward part of the Si II λ 1260 line is blended with a Ly α line at $z = 0.1205$. The intermediate ionization transition, Si III λ 1207, is blended to the red with the Galactic Si II λ 1304 line but it can be clearly separated. High ionization absorption is detected in Si IV λ 1393, 1402 and C IV λ 1548, 1550. The quality of the spectrum at the position of C IV λ 1548, 1550 is just higher than our survey threshold of $S/N = 5$. Because of this, it was difficult to assess whether additional components were detected in C IV, particularly one at ~ -50 km s $^{-1}$. The Ly α profile is broad and asymmetric, and is not centered on the profiles of the metal-line transitions. This system was published and studied by Jenkins et al. (2003).

3.1.5. System 5 – PG 1241+174, $z_{sys} = 0.5584$, MC low + MC high

This multiple-cloud weak low ionization system is presented in Figure 5. The Mg II doublet is detected in the Keck/HIRES spectrum. C II λ 1335 and Si II λ 1260 are not covered in the *HST*/STIS spectrum. The weaker Si II λ 1527 and Al II λ 1671 low ionization transitions are covered in the *HST*/STIS spectrum, but are not detected at 5σ . C IV λ 1548, 1550 is detected in the *HST*/STIS spectrum. Both the high and low ionization absorption profiles require multiple component fits. The C IV profiles are roughly centered on the low ionization profiles. Ly α is not covered by either spectrum. This system is reported in Churchill et al. (1999) and modeled by Ding et al. (2005).

3.1.6. System 6 – PG 1634+706, $z_{sys} = 0.6534$, SC low + MC high

This is a single-cloud weak low ionization absorption system with multiple components detected in C IV, as well as in Si IV. The system is shown in Figure 6. Si II λ 1260 and C II λ 1335 are detected in the *HST*/STIS data. Mg II λ 2796, 2803 is detected in the Keck/HIRES

spectrum. The strongest high ionization feature is centered on the low ionization cloud. $\text{Si III } \lambda 1207$ is detected, but is blended to the blue, possibly with $\text{Ly } \alpha$. $\text{Ly } \alpha$ is broad, and roughly centered on the high ionization absorption. Previous modeling by Charlton et al. (2003) shows separate low and high ionization phases.

3.1.7. System 7 – PG 1634+706, $z_{\text{sys}} = 0.8181$, SC low + SC high

This system is a single-cloud weak low ionization absorber with detected $\text{Mg II } \lambda\lambda 2796, 2803$, $\text{Si II } \lambda 1260$, and $\text{C II } \lambda 1335$ (see Figure 7). The $\text{Mg II } \lambda\lambda 2796, 2803$ were covered in the Keck/HIRES spectrum. Coverage of other transitions was provided through the *HST*/STIS dataset. The $\text{Ly } \alpha$ and C IV are centered on the Mg II cloud and do not have offset components. The $\text{Si III } \lambda 1207$ transition is blended, probably with $\text{Ly } \alpha$ at $z = 0.80412$. This system was modeled and discussed by Rigby et al. (2002) and Charlton et al. (2003). Although the low and high ionization absorption are centered at the same velocity, they must arise in two different phases (i.e., regions with different ionization parameters) (Charlton et al. 2003).

3.1.8. System 8 – PG 1248+401, $z_{\text{sys}} = 0.8548$, MC low + MC high

This system, shown in Figure 8, was detected in both *HST*/STIS and Keck/HIRES spectra. It shows complex multi-cloud structure in both the low and high ionization transitions. Higher ionization features are centered on the low ionization absorption, but do not trace it in strength. The $\text{C II } \lambda 1335$ profile is contaminated by an unknown feature at $\sim 160 \text{ km s}^{-1}$, and there is the possibility that other redward components are affected as well. The redward components of $\text{Si IV } \lambda 1393$ are heavily blended with Galactic $\text{Fe II } \lambda 2587$. $\text{N V } \lambda\lambda 1239, 1243$ may also be detected. The weaker line in that doublet is blended to the blue with $\text{Ly } \alpha$ at $z = 0.8951$. $\text{Ly } \alpha$ was not covered by the *HST*/STIS spectrum. This system was modeled and discussed by Ding et al. (2005).

3.1.9. System 9 – PG 1241+174, $z_{\text{sys}} = 0.8954$, SC low + SC high

This system, presented in Figure 9, is a single-cloud weak, low ionization system. The Mg II resonant doublet is detected in a Keck/HIRES spectrum. The C IV and Si IV doublets are detected in *HST*/STIS data, though $\text{Si IV } \lambda 1402$ is affected by an unidentified blend, possibly $\text{Ly } \alpha$. These high ionization profiles can be fit with single components, centered on the Mg II . $\text{C II } \lambda 1335$ is not detected in a noisy region of the *HST*/STIS spectrum. There

is a 5σ detection at the expected position of SiII λ 1260, however, based on photoionization models (Ding et al. 2005), the SiII λ 1260 seems too strong relative to MgII λ 2796 (see Table 3 for measurements and limits). The *HST*/STIS spectrum alone was not adequate to assess the classification of this system, but since we had access to Keck/HIRES data we were able to include it in our sample. Modeling of the system was complicated by an apparent offset ($\sim 7 \text{ km s}^{-1}$) between MgII and CIV. If the offset is neglected, the CIV could arise in the same phase with the MgII, but two-phase models are also consistent with the data (Ding et al. 2005).

3.1.10. System 10 – PG 1634+706, $z_{sys} = 0.9056$, SC low + MC high

This is a single-cloud weak low ionization system (see Figure 10). MgII $\lambda\lambda$ 2796, 2803 is detected in Keck/HIRES data. SiII λ 1260, CII λ 1335, and SiIII λ 1207 are detected in the *HST*/STIS spectrum. The SiII λ 1260 line is slightly blended to the blue with SiIII λ 1207 at $z = 0.9902$, but can be clearly separated. CIV $\lambda\lambda$ 1548, 1550 is detected at the velocity of the low ionization absorption, but the profiles are asymmetric, with an offset to the red. The OVI $\lambda\lambda$ 1032, 1038 doublet is covered and detected. Detailed discussions of this system appear in Rigby et al. (2002) and Charlton et al. (2003). Modeling showed that even the CIV that was centered on the low ionization absorption must come from a separate, higher ionization phase (Charlton et al. 2003).

3.1.11. System 11 – HS0624+6907, $z_{sys} = 0.0635$, MC high

This system, presented in Figure 11, is a high ionization only (high only) system. The CIV doublet is detected in three components. The high ionization absorption is confirmed for both components of SiIV $\lambda\lambda$ 1393, 1402, however, the detection of the weaker, redward component of SiIV 1402 is just above the 5σ limit. Absorption is also detected in SiIII λ 1207 for both components. The Ly α profile extends over the same velocities as the three high ionization components.

3.1.12. System 12 – PG1211+143, $z_{sys} = 0.0644$, MC high

This is a high only system (see Figure 12). It has multiple, but weak, CIV components. SiIV is not detected, however, there may be a detection of SiIII λ 1207. Ly α is saturated and it covers the same velocities as the CIV absorption.

3.1.13. *System 13 – HS0624+6907, $z_{sys} = 0.0757$, SC high*

The system, shown in Figure 13, is characterized by single-cloud high ionization absorption, which is detected as weak C IV $\lambda\lambda 1548, 1550$. Both of the strong low ionization indicators, C II $\lambda 1335$ and Si II $\lambda 1260$ are covered, but absorption is not detected. Lines of the C IV doublet are weak, with the minimum aligned in velocity with the broader Ly α .

3.1.14. *System 14 – PG1206+459, $z_{sys} = 0.7338$, MC high*

This system, presented in Figure 14, is a multiple-cloud high only system. The C IV $\lambda\lambda 1548, 1550$ doublet is detected in two components. The reddest component is the strongest. The bluest component is somewhat disputable. Its C IV $\lambda 1550$ transition is detected at the 3σ level, but it seems too weak compared to the matching component in C IV $\lambda 1548$. The C IV $\lambda 1548$ line is blended with the Si IV $\lambda 1393$ absorption from a system at $z = 0.9254$ (Ding et al. 2003). There is also an unidentified blend redward of the strongest component. The C IV $\lambda 1550$ line is also blended, to the blue, with the Si IV $\lambda 1393$ line of an absorption system at $z = 0.9276$, but these two lines can be cleanly separated. We use C IV $\lambda 1550$ to determine the two component fit listed in Table 4. C II $\lambda 1335$ is covered, but there is no absorption detected at that wavelength. Mg II $\lambda\lambda 2796, 2803$ is also not detected in the Keck/HIRES spectrum. Ly α is not covered in the HST/STIS spectrum.

3.1.15. *System 15 – PG1248+401, $z_{sys} = 0.7011$, SC high*

The system shown on 15 is a single-cloud high only absorption system. The only detected absorption is in C IV $\lambda\lambda 1548, 1550$. The Si IV $\lambda\lambda 1393, 1402$ doublet is covered, but there is no detected absorption. The wavelengths at the expected position of Si IV $\lambda 1402$ are contaminated by Ly α at $z = 0.9635$. Ly α at z_{sys} is not covered in the HST/STIS spectrum.

3.1.16. *System 16 – PG1630+377, $z_{sys} = 0.9143$, MC high*

This system, shown in Figure 16, has a C IV doublet that can be adequately fit with three components. Because the C IV $\lambda 1548$ profile is heavily blended to the blue, our fit to the bluer part of the profile was determined only using C IV $\lambda 1551$. The expected position of C II $\lambda 1335$ is affected by an unidentified blend, but there is a feature detected at 3σ at the wavelength of the Si II $\lambda 1260$ line, which is centered on the strongest C IV component.

We classify this system as high only, however this classification is uncertain, with a low ionization phase being possible. There are also detections of Si III λ 1207 and of the Si IV and NV doublets. The NV λ 1243 line is blended with Ly α at $z = 0.9573$. The Ly α profile is not symmetric but is extended to the red of the strongest CIV component, presumably due to a contribution from the cloud that produced the redward CIV component.

3.2. Systems That Failed To Pass The Survey Requirements

For some systems in our dataset we did not have the required coverage of CIV λ 1548, 1550 or of low ionization transitions. In that case we could sometimes supplement our dataset with the *HST*/FOS Archive. However, since the resolution of FOS is insufficient for our study of CIV kinematics, we exclude them from our main survey. For some systems, CIV was covered in a *HST*/STIS dataset, however that region had S/N less than our requirement of 5 per pixel. We excluded the following systems from our survey: $z = 0.1385$ toward PG 1116+215, $z = 0.7390$ toward PKS 0232-04, $z = 0.8313$ toward HS 0810+2554, $z = 0.5648$ toward PG 1248+401, $z = 0.7290$, 1.3250, and 1.3430 toward PG 0117+210, $z = 0.9343$ toward PG 1206+459, and $z = 1.0400$ toward PG1634+706.

4. Results

We classify systems based upon whether they have detected low and/or high ionization transitions. Specifically, we define “weak low ionization + high ionization” (low + high), “low ionization only” (low only), and “high ionization only” (high only) systems. Here we consider the relative numbers of these three types of systems in our unbiased survey.

Nine of the systems found in our survey have both high and low ionization transitions detected (six have single-cloud low ionization components and three have multiple), six systems are high ionization only, and one system has only low ionization absorption detected. Table 3 lists the equivalent widths of key transitions for these three categories of systems. Four of the six single-cloud low + high systems have multiple clouds in their high ionization phases. Four of the six high ionization only systems have multiple-component clouds.

4.1. Comparison of CIV Profiles – Kinematics of CIV

In Figure 17, we compare the kinematic profiles of CIV between the different classes of systems. All but one system, which only has low ionization absorption detected (the

$z = 0.0053$ system toward 3C 273), have high ionization absorption at the same velocity as their low ionization absorption. In some cases, there is only one component detected in CIV, but in most cases there are additional CIV components offset by 5-150 km s⁻¹. The CIV component that is centered on the low ionization absorption is always stronger than the offset CIV component/s. In one case (the $z = 0.0057$ system toward RX J1230.8+0115) one of the two low ionization components does not have detected CIV absorption. The high only category of absorbers also contains both single and multiple component CIV profiles.

The kinematic spreads of the CIV in high only systems are similar to those of the CIV of systems in the low + high ionization category. There is, however, an important difference between the CIV profiles of high only and low + high ionization systems. To illustrate this, we performed Voigt profile fits to the CIV profiles for these systems and we present the results in Table 4. Figure 18 shows the CIV column densities for the individual Voigt profile components in each system, allowing comparison between the CIV in low + high and high only systems. Although there is some overlap, high only systems tend to have component CIV column densities less than those of low + high ionization systems. A Kolmogorov-Smirnov (KS) test between the two samples yields only a 2.7% chance that they are drawn from the same distribution.

The strongest CIV components in the high only systems generally fall in the same column density range as the offset CIV components of low + high systems. A Kolmogorov-Smirnov (KS) test between the distributions of maximum CIV component column densities for these two samples yields a 14% chance that they are drawn from the same distribution, which is not a very significant difference. However, the samples are small, and if System 16 is considered to be a low + high system (possible because of the 3σ detection of SiII λ 1260, as discussed in § 3.1.16), there is only a 4.1% chance that they are drawn from the same distribution.

4.2. Comparison of Ly α Profiles

We also consider the relationship between the Ly α profiles and the low ionization and CIV profiles for our systems. The Ly α profiles are plotted along with those of the other transitions in Figures 1–16. The Ly α profiles encompass the full velocity range of the metal line absorption. In many cases, the Ly α profiles are clearly not centered on the low ionization absorption. When there are offset CIV components, the Ly α profile is asymmetric in the same sense (see Figures 1 – 16). One example is the $z = 0.9055$ system toward PG 1634 + 706 (see Figure 10), in which there is an offset blended CIV component to the red of the component centered on MgII. Another example, in which the offset CIV components are distinct, is the

$z = 0.6534$ system toward PG 1634 + 706 (see Figure 6).

In principle, the Ly α profile related to a given system might be broader because the gas (either low or high ionization) has a lower metallicity. Alternatively, the Ly α profile might be broader because of a large kinematic spread of the CIV components, which combine their associated Ly α absorption to produce the overall Ly α profile. To test between these two ideas, we consider whether the kinematic spread of Ly α is more closely correlated with the equivalent width of CIV or with the kinematic spread of CIV. For fixed Ly α , we would expect $W_r(\text{CIV}\lambda 1548)$ to be larger for a higher metallicity. Figure 19 shows a closer correlation between $\omega(\text{CIV}\lambda 1548)$ and $\omega(\text{Ly}\alpha)$. To assess the significance of this apparent difference, we conducted the Student’s t-Test between two dependent correlations (Chen & Popovich 2002). We found that, although both sets of values are highly correlated, the correlation between $\omega(\text{CIV}\lambda 1548)$ and $\omega(\text{Ly}\alpha)$ is more significant at the 3.0 σ level ($t = 3.51$, yielding a probability of less than 1%, for eight degrees of freedom, that $\omega(\text{CIV}\lambda 1548)$ and $W_r(\text{CIV}\lambda 1548)$ are more correlated). The kinematics of the CIV absorbing gas appears to be a significant factor in determining the strength of the Ly α absorption.

5. Discussion of Geometry

Considering the above results and the physical properties of weak low ionization absorption systems, derived from photoionization models, we will now discuss general constraints on their geometry. Our goal is to better understand the nature of the structures in which the low and high ionization absorption arises. Here we summarize briefly the important observational constraints that must be satisfied:

1. There are just six high only systems found in our survey sample, which contains six single-cloud weak low ionization systems. One additional system is found with single-cloud weak low ionization absorption, but with no detected high ionization absorption. In comparison, three multiple cloud weak low ionization systems were found, each with detected high ionization absorption.
2. For low + high ionization systems, the strongest CIV absorption is aligned with the strongest low ionization absorption.
3. The CIV profiles for both the high only and low + high ionization systems have a similar distribution of kinematic spreads. For both categories, some systems have single components of high ionization absorption and some have multiple components.

4. The CIV absorption tends to be similar, but somewhat weaker, for high only systems than for low + high ionization systems, both in the strongest CIV component and in outlying CIV components.
5. The Ly α absorption is very closely related to the kinematics of the CIV profiles, more so than it is to the low ionization absorption.

Our discussion will focus on the origin of single-cloud weak low ionization systems with properties adopted from Rigby et al. (2002) and Charlton et al. (2003). We choose this subset because many multiple-cloud weak low ionization systems may have a different physical origin, as described in § 1. The structures that produce single-cloud weak low ionization absorption were found to have thicknesses ranging from ~ 1 pc – 100 pc, and densities of ~ 0.01 cm $^{-3}$. The narrow line profiles imply a velocity dispersion of ~ 5 km s $^{-1}$, which corresponds to a virial mass of $\sim 3 \times 10^4$ M $_{\odot}$ for a 10 pc structure. This is a considerably larger mass than the gas mass in a spherical structure with density 0.01 cm $^{-3}$ and radius 10 pc. This suggests confinement by dark matter mini-halos or by a stellar structure such as a galaxy or star cluster. The high ionization absorption related to the same systems is produced in larger structures, with larger velocity dispersions and with sizes of ~ 1 kpc, which could be related to confinement.

In our survey, we found both low+high ionization systems and high only systems. Point 4 above implies that there are real differences, either in degree or kind, between the low + high systems and the high only systems. There appear to be two different kinds of CIV structures, those with low ionization regions of higher density covering most of their area, and those without these higher density regions along the line of sight. In this way we can explain the high only systems and the weaker, offset components in low + high ionization systems as a different or less extreme population than the central component of a low + high ionization system. In this population, eg., the total hydrogen column density might have been lower so that a higher density substructure did not collapse in the region. The data would also be consistent with a CIV column density, for clustered clouds, that tends to decrease outward from a central cloud in which MgII absorption arises. Without such a fall-off, a model could not explain the observed difference between the $N(\text{CIV})$ of the component centered on the low ionization absorption and the offset CIV and high only system components.

Guided by these general principles, we now consider the most basic “toy-model” scenarios for the origins of the low and high ionization absorption in single-cloud weak low ionization absorbers:

1. *Single spherical low ionization region inside spherical high ionization region*— The first, simplest model to consider, based on derived sizes, is one in which a ~ 10 pc low

ionization cloud is embedded in a ~ 1 kpc higher ionization halo. This model would give rise to $\sim 10^4 \times$ more high only systems than single-cloud low + high systems. We observe a ratio of only 6/6, such a severe discrepancy that this model is easily ruled out.

2. *Multiple spherical low ionization regions inside spherical high ionization region—*

The previous model can be improved by using multiple spherical low ionization clouds inside a high ionization halo. In order to produce the derived ratio of high only to low + high ionization systems, the covering factor should be $C_f \sim 0.5$. This would imply a probability of $\sim C_f^2 = 0.25$ of passing through two of the low ionization clouds along a given line of sight. This is not inconsistent with the data, since some fraction of the $\sim 33\%$ of weak low ionization systems that have multiple clouds could be produced in this way. However, in order to produce $C_f \sim 0.5$, there would need to be ~ 5000 low ionization structures with a size of ~ 10 pc in each ~ 1 kpc high ionization halo. If the ratio of sizes of low to high ionization structures was instead 1/1000, there would have to be a factor of $100 \times$ more small clouds per large halo. The average spacing between the small clouds in the halo would be 94 pc for the first choice of size ratio, and 20 pc for the second. This is not much larger than the cloud size, and seems a very contrived situation. Without a physical model to support such a scenario, we consider this model unlikely, though it is not strictly ruled out. Also, this simple model does not produce offset high ionization components as are found in our survey.

We can modify this model to attempt to explain the observed offset CIV components. In this modified model, separate high ionization halos would give rise to these components. These halos would have lower covering factors for low ionization absorption than the “main” halo (the one giving rise to low ionization absorption). Since we are constrained to have an average of one offset component per low + high system, roughly half of the sky, looking out from the main halo, would need to be covered by the separate high ionization halos. In this case, looking from a large distance at the clustered group of halos, an observer would see a covering factor for the separate high ionization halos that greatly exceeds that from the main halo. Adding the separate high ionization halos would therefore produce more high only systems than we observe, so that in fact we have not improved on the model after all.

3. *Low ionization shell surrounding high ionization shell—*

Alternatively, we now consider a situation where a low ionization shell surrounds an interior shell of high ionization gas. In order not to exceed the number of multiple-cloud weak low ionization absorbers (relative to single-cloud), the low ionization shell should be fragmented. This fragmented shell must cover roughly 33% of the surface area of

the bubble (assuming small fragments), so that it is more typical to pass through low ionization absorption on only one side of the interior region.

With only a single such “bubble”, there is no clear explanation for offset high ionization components for this model. We might expect either one or two high ionization components, depending on the covering factor of the high ionization shell. It is not clear that a component without detected low ionization absorption would have a smaller CIV column density than one which did, since it would come from a different layer. To account for the offset components, we can consider clustering of “bubbles”. However, such a model suffers from the same problems as our similar attempts to modify Model 2, in that the additional bubbles will produce too large a ratio of high only to low + high ionization systems.

4. *Network of filaments/sheets which gives rise to high ionization absorption, with embedded low ionization condensations—*

We finally consider a model in which low ionization condensations are embedded in filaments and/or sheets which give rise to high ionization absorption. The overall covering factor of the low ionization regions (relative to high ionization regions) must be $C_f \sim 0.5$ to explain the observed ratio of high only to low + high ionization systems. In view of the small low ionization cloud thicknesses, a filamentary/sheetlike geometry is a straightforward way to produce the observed covering factor, without requiring huge numbers of separate spherical clouds. The lines of sight through filaments/sheets that do not give rise to low ionization absorption are typically characterized by smaller $N(\text{CIV})$ values than those that do. These smaller $N(\text{CIV})$ structures would give rise both to high only systems and to the offset high ionization components of low + high systems. In such a model, we would expect the number of high ionization components to be similar for the two categories of systems, as is observed. We favor this model because it naturally produces all of the results derived from our survey.

6. Connection to Physical Models

In the previous discussion, we intentionally avoided consideration of the physical models that might give rise to weak low ionization absorption. Instead, we focused on basic geometric possibilities, some of which we were able to exclude based upon results of our survey. Now, we consider the connections between these geometries and the possible mechanisms for the origin of the absorbing clouds.

Based upon photoionization modeling, Rigby et al. (2002) sketched out three classes of

physical models, for single-cloud weak low ionization absorbers, that were consistent with the data. In one class, the weak MgII absorption arose from the traces of gas remaining in a Population III, pre-galactic or dwarf galaxy star cluster, with the high ionization absorption coming from gas bound in the surrounding dark matter halo. In the second class of models, the weak MgII absorption is produced in fragments of shells from Type Ia supernovae, housed in a surrounding dark matter halo. In the third class of models, the absorption arises in high velocity cloud structures that are typically found in galaxy groups.

The most basic form of a star cluster model for weak MgII absorption matches Scenario 1 in § 5. If there is only one star cluster per spherical dark matter halo (which produces the high ionization absorption) then this model is clearly ruled out by cross-section arguments. The idea of having many star clusters per dark matter halo is described by Scenario 2. It does not seem reasonable to have such a tight packing of star clusters as would be required. Furthermore, this type of model cannot be consistent with the small number of high only systems compared to low + high ionization systems. Although it agreed quite well with velocity dispersions and derived cloud sizes of the low and high ionization phases, it appears that star cluster models are ruled out.

The next model we consider is one in which supernova remnant shells produce the weak, low ionization absorption, as described in Scenario 3 in § 5. The CIV absorption is most likely to be in a concentric shell inside of the low ionization shell. It is not unreasonable that a supernova remnant would have a patchy shell structure in order to produce the 33% covering of the surface area as required by our survey results. However, for this scenario, as with Scenario 2, we were unable to envision a clustering of remnants that would appropriately produce observed offset high ionization absorption without overproducing high only systems.

Another physical picture to which Scenario 2 applies is weak MgII absorption arising in superwinds, as suggested by Stocke et al. (2004) and Rosenberg et al. (2003) as an explanation for absorption coincidence (low ionization and HI at similar velocities) between the $z = 0.0057$ system toward RXJ 1230.8+0155 and the nearby $z = 0.0052$ system toward 3C 273, separated by $350h^{-1}$ kpc. Support for this hypothesis is provided by the detection of a post-starburst galaxy at an impact parameter of $71h^{-1}$ kpc from the 3C 273 line of sight. In that specific case, it is hard to explain the absence of CIV absorption along the 3C 273 line of sight in the context of a superwind cone/shell with a series of ionized layers. However, more generally, the superwind idea is compelling since low ionization absorption is observed in nearby superbubbles/winds (Heckman 2001). Clearly, such winds must present a non-negligible cross section for absorption. Zonak et al. (2004) have suggested that they may be responsible for some multiple-cloud weak MgII absorbers. However, we argue here that there are problems with using them to explain single-cloud weak low ionization absorbers based

upon our considerations of Scenario 2. Again, offset components require clustered additional bubbles/winds which would produce too many high only systems. This leads us to focus primarily on Scenario 4.

There are similarities between recent models for high velocity cloud structure in the Local Group (Fox et al. 2005; Sembach et al. 2002) and Scenario 4. Fox et al. (2005) describes low ionization clouds sweeping through a hot medium (either a galactic corona or an intergalactic medium) to produce high ionization absorption in a conductive or turbulent interface. The Local Group high velocity clouds cover large areas of the sky and exhibit similar absorption strengths and coherent motions over large angular scales (Wakker et al. 2003; Sembach et al. 2002; Fox et al. 2005), suggesting sheetlike geometries. We found that Scenario 4 was consistent with our survey results. Rigby et al. (2002) stated that the single-cloud weak low ionization absorbers with large FeII column densities could not be produced by high velocity cloud analogs. This was because the high iron abundance that was required implied “in situ” star formation rather than ejection from Type II SNe. Although present-day star formation is limited in the Milky Way high velocity clouds, past star formation is not ruled out, making a high velocity cloud model for single-cloud weak low ionization absorbers more likely. We also note that OVI absorption, which we have not examined in our survey, should accompany CIV absorption for analogs to Local Group high velocity clouds. Although Scenario 4 applies to high velocity cloud models, it also applies more generally. It remains to be understood how high velocity cloud models fit in with the “bigger picture” of the cosmic web of filaments and sheets expected from cosmological simulations.

Another related possible scenario has weak low ionization absorption arising in collapsed regions in material in tidal debris or as a result of ram pressure due to high velocity inflow through a hot intracluster or intragroup medium. Although it may not be common in the present-day universe, there is at least one example of widespread star formation in a group of galaxies moving through the rich cluster, A1367 (Sakai et al. 2002). The star formation is taking place in many dwarf galaxies and in intergalactic HII regions, and it is of particular interest that the metallicities in these star-forming regions are close to the solar value (Sakai et al. 2002), despite their dwarf environments. This implies that weak low ionization absorbers could also arise in dwarfs, or at least in certain regions of some types of dwarfs. A faded population of such objects from similar processes acting at high redshifts could present non-negligible cross-section. The geometry of the remnant gas is uncertain, but could be consistent with our Scenario 4. This idea is not necessarily distinct from the origin of high velocity clouds or from the general cosmic web.

The overlap between the single-cloud weak low ionization absorbers and the population of CIV absorbers at low redshift is substantial. Thus information about the physical

environments of CIV absorbers could provide clues to the nature of the single-cloud weak low ionization absorbers. By connecting absorption features with nearby galaxies, Chen, Lanzetta, & Webb (2001) found that galaxies are surrounded by CIV halos with an extent of $R \sim 100h^{-1}(L/L_B)^{0.5}$ kpc at $W_r(1548) \sim 0.1 \text{ \AA}$. They favored a scenario in which these CIV halos were produced by gas stripped from accreting satellite galaxies. Also, it follows from their Figure 3 that all absorbers with detected $W_r(1548) > 0.1 \text{ \AA}$ were found within $R \sim 100h^{-1}(L/L_B)^{0.5}$ kpc. There are many additional galaxies at larger impact parameters that have only 3σ limits on $W_r(1548)$, most of which fall between 0.1-0.2 \AA . However, many of these may lie significantly below that detection limit.

In our sample, 5/6 of the low + high single-cloud weak low ionization and 4/6 of the high only systems have $W(1548) > 0.1 \text{ \AA}$. Based upon the results of Chen, Lanzetta, & Webb (2001), we would therefore expect that the majority of these CIV absorbers are produced within $R \sim 100h^{-1}(L/L_B)^{0.5}$ kpc of a galaxy. It also follows that a significant fraction of the single-cloud weak low ionization absorbers would be within this radius of a galaxy. The fact that we did not find a large number of high only systems implies that a large fraction of the CIV absorption regions around galaxies also produces single cloud weak low ionization absorption. This loose association between weak low ionization absorption and luminous galaxies is consistent with recent observations in individual cases (Churchill et al. 2005), and is not inconsistent with previous claims that close associations are uncommon (Rigby et al. 2002).

Our study indicates that, although weak MgII absorbers are not directly associated with luminous galaxies, they are in their environments. However, our statistics are relatively small, and more ultra-violet spectra are needed to increase our understanding of the low redshift weak low ionization absorber population. Based on the geometrical considerations in § 5, we favor a general model in which spherical or flattened low ionization condensations or transient regions inhabit sheets and/or filaments which give rise to high ionization. In this model, the covering factor of the high ionization region by low ionization condensations would need to be large, close to 50%. This type of origin in such a cosmic web is not necessarily different from an origin in satellite dwarf galaxies or failed dwarf galaxies, or in high velocity clouds, which are themselves components of the web. Single-cloud weak low ionization absorption requires condensations, apart from luminous galaxies, in which stars have formed. Such regions could be otherwise undetected components of the cosmic web, yet to be resolved in numerical simulations. However, they could also be related to known structures with uncertain origin, like the high velocity clouds, that are already known to be clustered around galaxies. In any case, we would expect collapse and solar metallicity star formation products to be most likely in the larger secondary potential wells that would exist in the cosmic web in the vicinity of luminous galaxies.

Thanks to C. Churchill for providing his HIRES/Keck I spectra. We are also grateful to B. Jannuzi and S. Kirhakos for providing fully reduced FOS spectra with continuum fits. This work was enhanced by our conversations with C. Churchill, M. Ćirković, A. Narayanan, and T. Tripp. This research was funded by NASA under grant NAG5-6399 NNG04GE73G and by NSF under grant AST 04-07138. J.R.M. and R.S.L. were partially funded by the NSF REU program.

REFERENCES

- Bergeron, J., & Boissé, P. 1991, *A&A*, 243, 344
- Bergeron, J., Cristiani, S., & Shaver, P. A. 1992, *A&A*, 257, 417
- Brown, T., et al. 2002, *HST STIS Data Handbook*, version 4.0, ed. B. Mobasher (Baltimore; STScI)
- Bruzual, A. G., & Charlot, S. 1993, *ApJ*, 405, 538
- Charlton, J. C., & Churchill, C. W. 1998, *ApJ*, 499, 181
- Charlton, J. C., Ding, J., Zonak, S. G., Churchill, C. W., Bond, N. A., & Rigby, J. R. 2003, *ApJ*, 589, 311
- Chen, H. W., Lanzetta, K. M., & Webb, J. K. 2001, *ApJ*, 556, 158
- Chen, P. Y., & Popovich, P. M. 2002, *Correlation: Parametric and Nonparametric Measures* (Thousand Oaks, CA: Sage Publications)
- Churchill, C. W., Kacprzak, G. G., & Steidel, C. C. 2005, *ArXiv Astrophysics e-prints*, arXiv:astro-ph/0504392
- Churchill, C. W., Mellon, R. R., Charlton, J. C., Jannuzi, B. T., Kirhakos, S., Steidel, C. C., & Schneider, D. 2000, *ApJ*, 543, 577
- Churchill, C. W., Rigby, J. R., Charlton, J. C., & Vogt, S. S. 1999, *ApJS*, 120, 51
- Churchill, C. W., & Vogt, S. S. 2001, *AJ*, 122, 679
- Churchill, C. W., Vogt, S. S., & Charlton, J. C. 2003, *AJ*, 125, 98
- Ćirković, M. M., Samurović, S., & Djorić, A. 2000, *ASS*, 274, 867
- Ding, J., Charlton, J. C., & Churchill, C. W. 2005, *ApJ*, 621, 615
- Ding, J., Charlton, J. C., Churchill, C. W., & Palma, C. 2003, *ApJ*, 590, 746
- Fox, A. J., Wakker, B. P., Savage, B. D., Tripp, T. M., Sembach, K. R., & Bland-Hawthorn, J. 2005, *ArXiv Astrophysics e-prints*, arXiv:astro-ph/0505299
- Heckman, T. M. 2001, *ArXiv Astrophysics e-prints*, arXiv:astro-ph/0107438
- Jenkins, E. B., Bowen, D. V., Tripp, T. M., Sembach, K. R., Leighly, K. M., Halpern, J. P., & Lauroesch, J. T. 2003, *AJ*, 125, 2824

- Kimble, R. A., et al. 1998, *ApJ*, 492, L83
- Le Brun, V., Bergeron, J., Boissé, P., & Christian, C. 1993, *A&A*, 279, 33
- Masiero, J. R., Charlton, J. C., Ding, J., & Churchill, C. W. 2005, *ApJ*, 623, 57
- Narayanan, A., Charlton, J. C., Masiero, J. R., & Lynch, R. 2005, *ApJ*, 632, 92
- Nestor, D. B., Turnshek, D. A., & Rao, S. M. 2005, *ApJ*, 628, 637
- Petitjean, P., & Bergeron, J. 1990, *A&A*, 231, 309
- Rigby, J. R., Charlton, J. C. & Churchill, C. W., 2002, *ApJ*, 565, 743
- Rosenberg, J. L., Ganguly, R., Giroux, M. L., & Stocke, J. T. 2003, *ApJ*, in press
- Savage, B. D., Sembach, K. R., & Lu, L. 1997, *AJ*, 113, 2158
- Sakai, S., Kennicutt, R., van der Hulst, J. M., & Moss, C. 2002, *ArXiv Astrophysics e-prints*, arXiv:astro-ph/0207041
- Sembach, K. R., et al. 2002, *ArXiv Astrophysics e-prints*, arXiv:astro-ph/0207562
- Schneider, D. P., et al. 1993, *ApJS*, 87, 45
- Steidel, C.C. 1995, in *QSO Absorption Lines*, ed. G. Meylan (Garching : Springer Verlag), 139
- Steidel, C. C., Dickinson, M., Meyer, D. M., Adelberger, K. L., & Sembach, K. R. 1997, *ApJ*, 480, 568
- Steidel, C. C., Dickinson, M. & Persson, E. 1994, *ApJ*, 437, L75
- Steidel, C. C., Kollmeier, J. A., Shapley, A. E., Churchill, C. W., Dickinson, M., & Pettini, M. 2002, *ApJ*, 570, 526
- Steidel, C. C., & Sargent, W. L. W. 1992, *ApJS*, 80, 1
- Stocke, J. T., Keeney, B. A., McLin, B. M., Rosenberg, J. L., Weymann, R. J. & Giroux, M. L. 2004, *ApJ*, 609, 94
- Sutherland, R.S., & Dopita, M.A., 1993, *ApJS*, 88, 253
- Tripp, T. M., et al. 2002, *ApJ*, 575, 697
- Vogt, S. S. et al. 1994, *Proc. SPIE*, 2198, 362

Wakker, B. P., et al. 2003, ApJS, 146, 1

Zonak, S. G., Charlton, J. C., Ding, J. & Churchill, C. W. 2004, ApJ, 606, 196

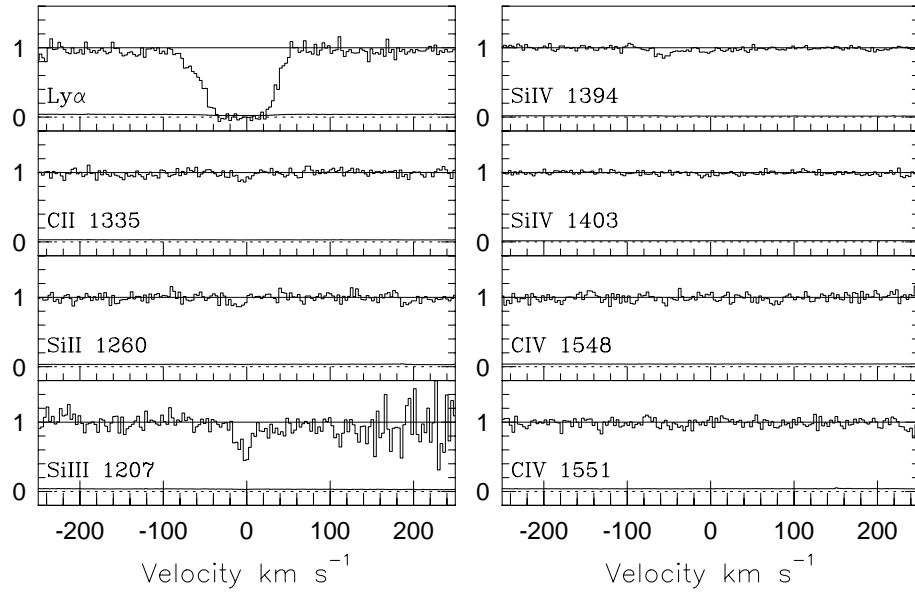


Fig. 1.— Absorption profiles for key transitions, displayed as normalized flux vs. velocity, for the $z = 0.0052$ system toward the quasar 3C 273. All data are from an *HST*/STIS spectrum.

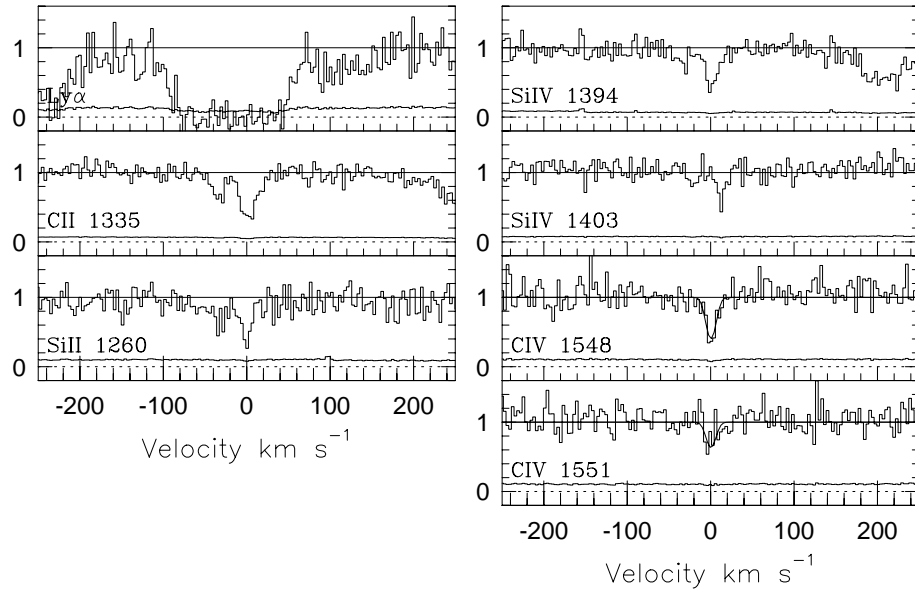


Fig. 2.— Same as Figure 1, for the $z = 0.0057$ system toward RXJ 1230.8+0115 quasar spectrum. Results of our Voigt profile fit to CIV $\lambda\lambda 1548, 1550$ are superimposed as a solid curve on the data.

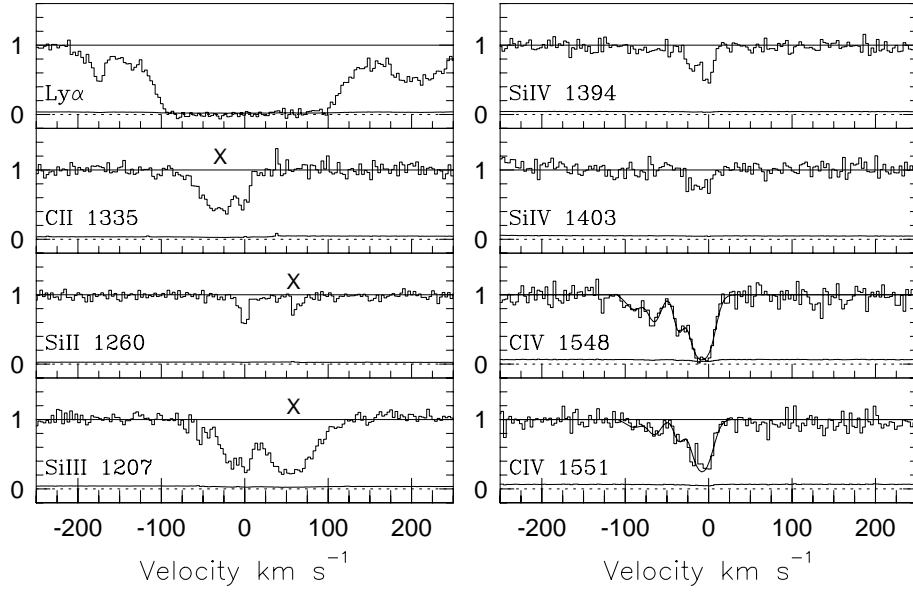


Fig. 3.— Same as Figure 2, for the $z = 0.0512$ system toward PG 1211+143. The $\text{C II } \lambda 1335$ transition is blended to the blue with Galactic Si IV . Si III is also detected, but it is blended with a $\text{Ly } \alpha$ line at $z = 0.0435$. Blends are marked with the symbol “X”.

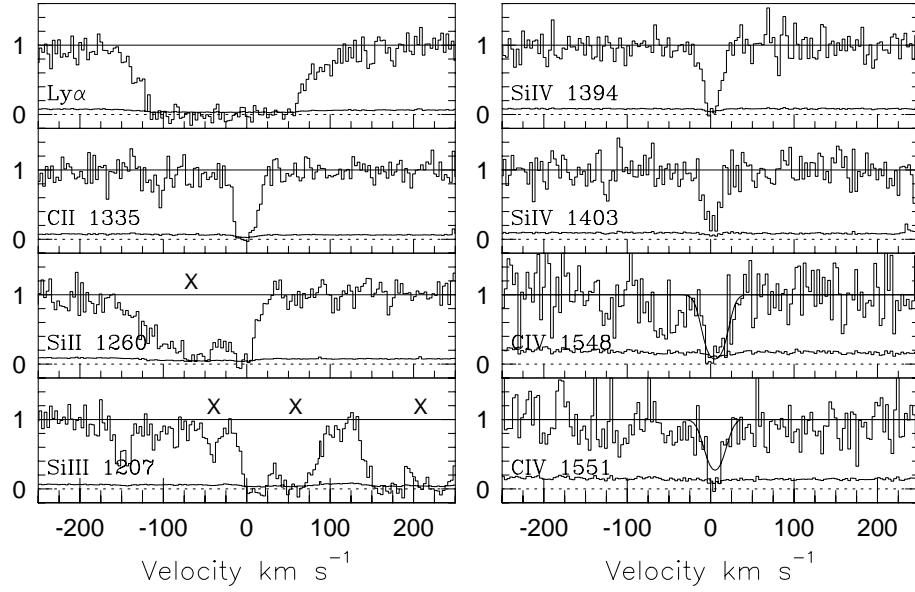


Fig. 4.— Absorption profiles for the $z = 0.0809$ system in the line of sight towards quasar PHL 1811, as in Figure 2. The $\text{SiIII}\lambda 1207$ feature is blended to the red with Galactic $\text{SiII}\lambda 1304$ line. Blends are marked with the symbol “X”.

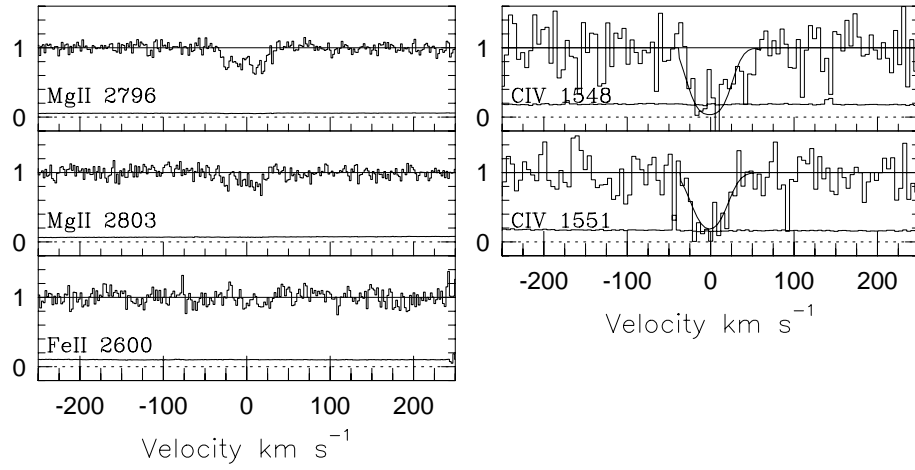


Fig. 5.— The multiple-cloud weak low ionization system at $z = 0.5584$ in PG 1241+174 quasar spectra. The low ionization transitions, FeII and MgII $\lambda\lambda 2796, 2803$, are covered by a Keck/HIRES spectrum, and other transitions by a *HST*/STIS spectrum. Our Voigt profile fit to CIV $\lambda\lambda 1548, 1550$ is superimposed on those data.

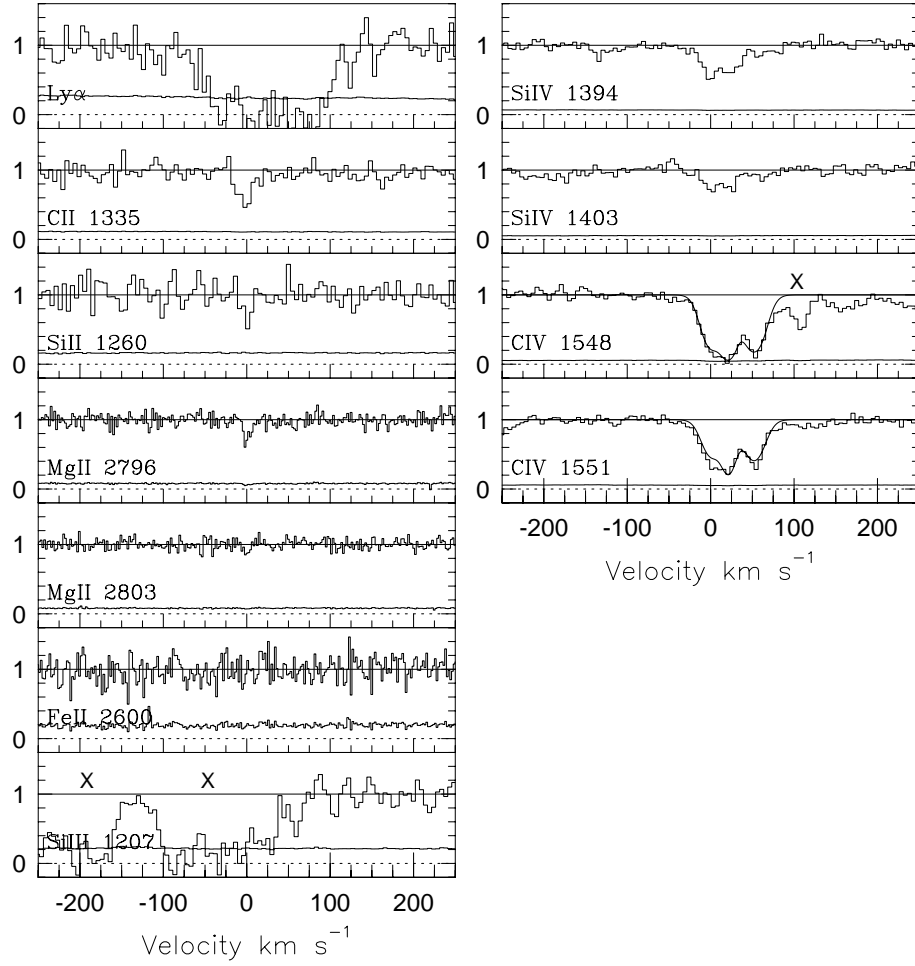


Fig. 6.— Same as Figure 5, but for the system at $z = 0.6534$ in spectrum of PG 1634+706. Blends are marked with the symbol “X”.

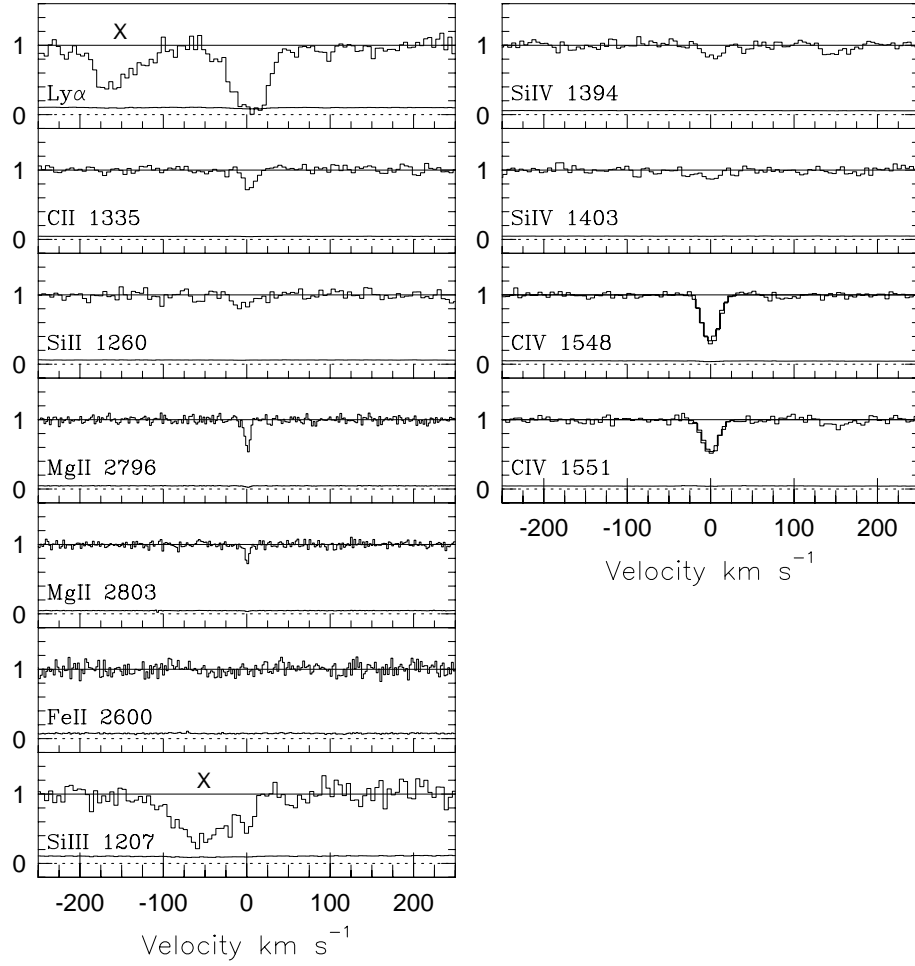


Fig. 7.— Same as Figure 5, but the system $z = 0.8181$ towards the quasar PG 1634+706. Blends are marked with the symbol “X”.

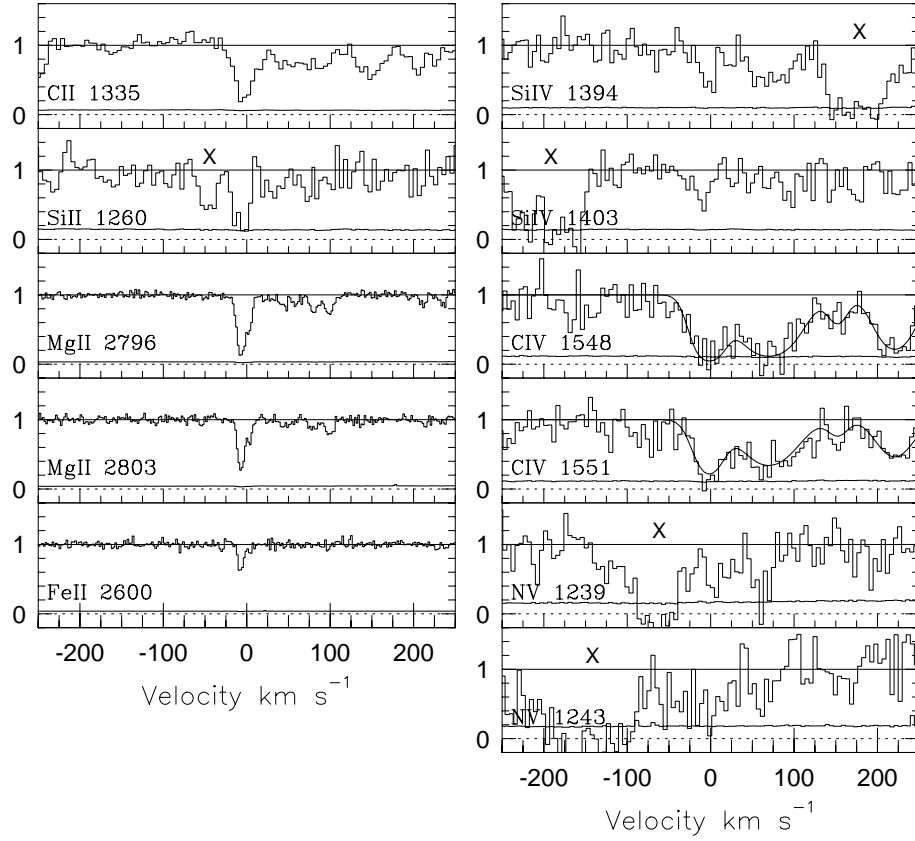


Fig. 8.— Same as Figure 5, but for the system at $z = 0.8545$ towards the quasar PG 1248+401. Blends are marked with the symbol “X”.

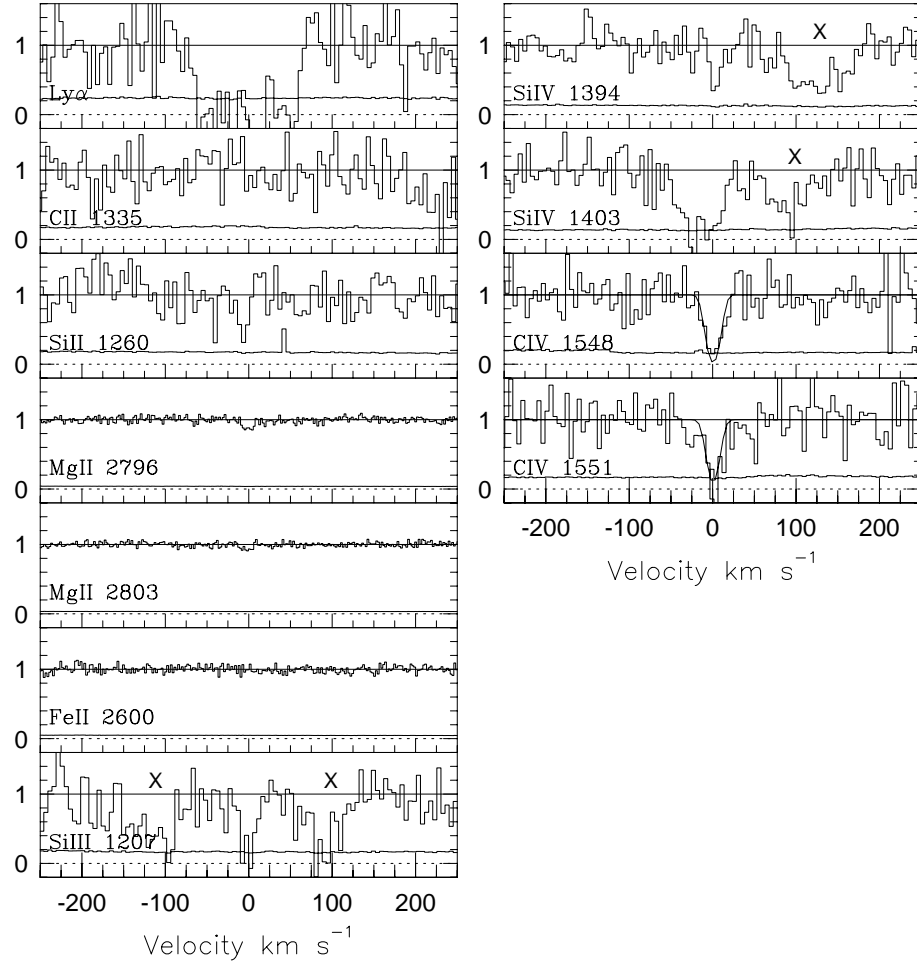


Fig. 9.— Same as Figure 5, but for the system at $z = 0.8954$ in the line of sight of the quasar PG 1241+174. Blends are marked with the symbol “X”.

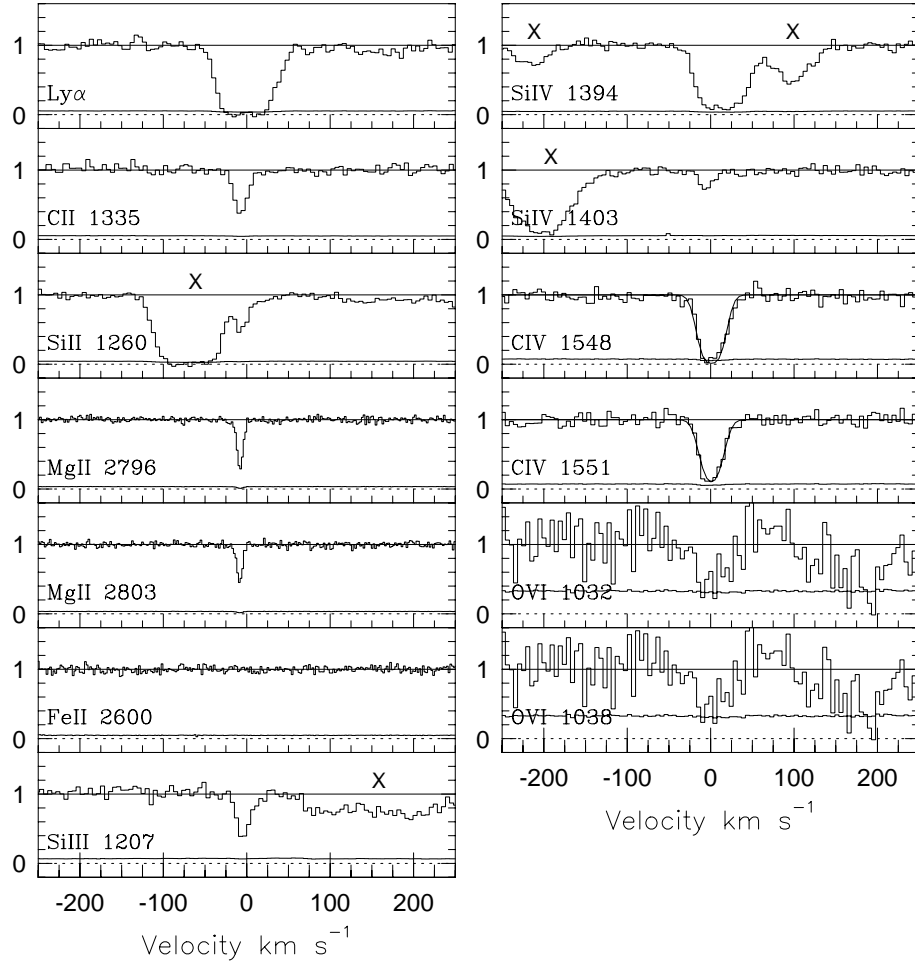


Fig. 10.— Same as Figure 5, but for the system $z = 0.9056$ towards the quasar PG 1634+706. Blends are marked with the symbol “X”.

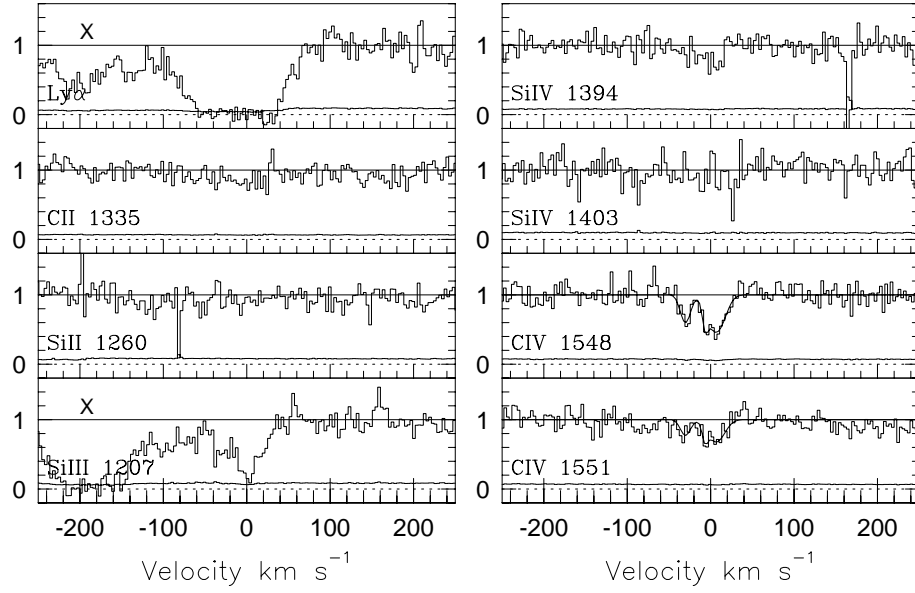


Fig. 11.— Same as Figure 2, but for the system $z_{sys} = 0.0634$ towards the quasar HS 0624. Blends are marked with the symbol “X”.

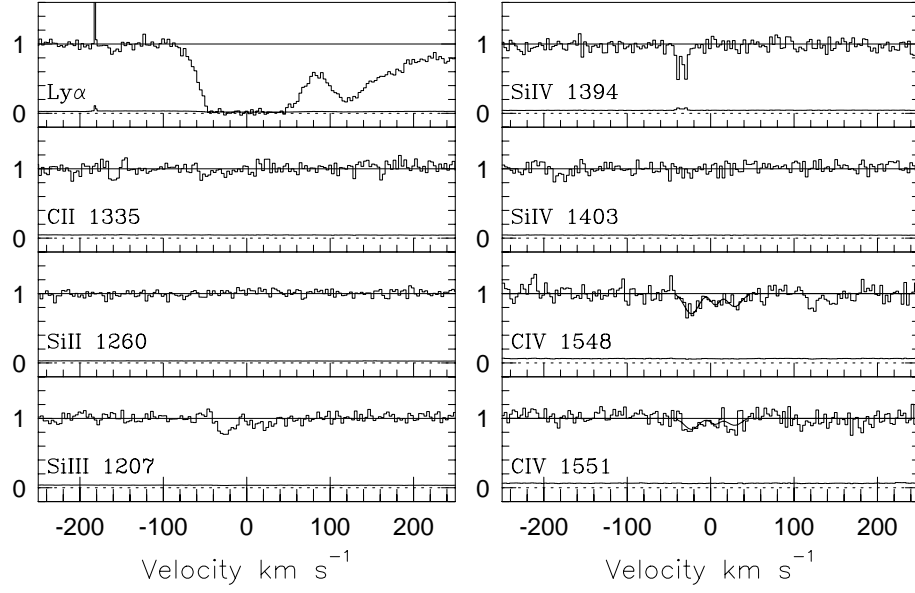


Fig. 12.— Same as Figure 2, but for the multiple-cloud high only ionization absorption system towards the quasar PG1211+143 at $z_{sys} = 0.0644$.

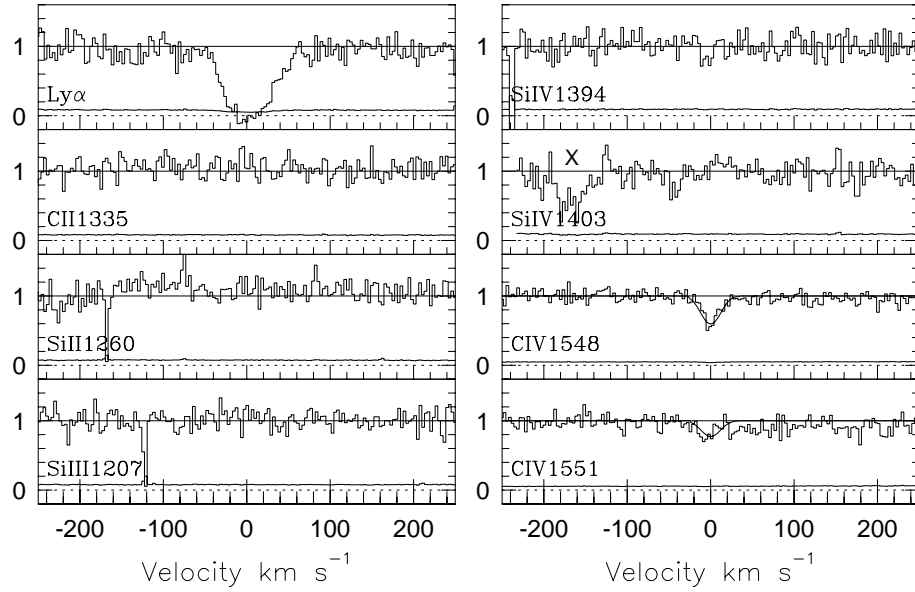


Fig. 13.— Same as the Figure 2, but for the single-cloud high ionization only system $z_{sys} = 0.0757$ detected in the spectrum of quasar HS0624+6907. Blends are marked with the symbol “X”.

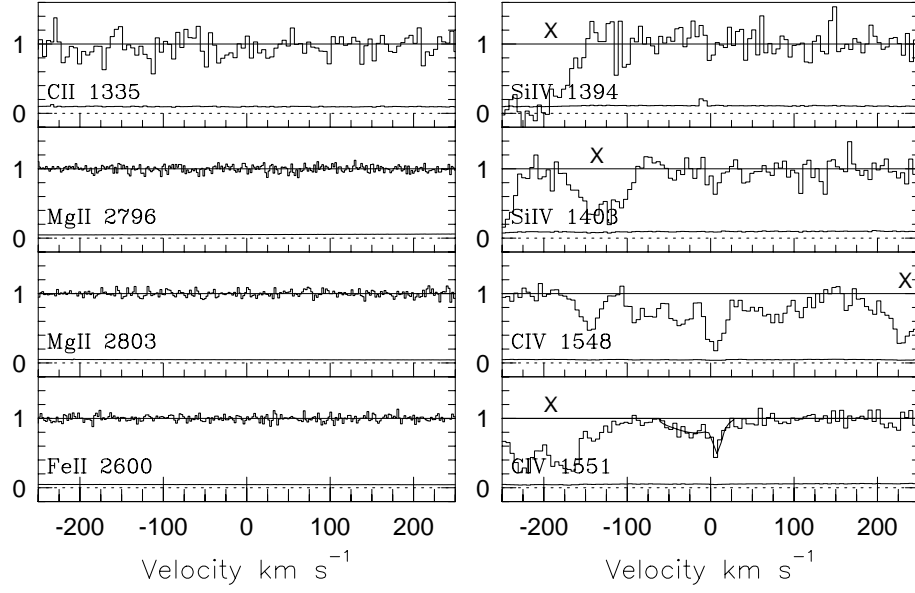


Fig. 14.— Same as the Figure 5, but for the multiple-cloud high ionization only system toward the quasar PG1206+459 at $z_{sys} = 0.7338$. Blends are marked with the symbol “X”.

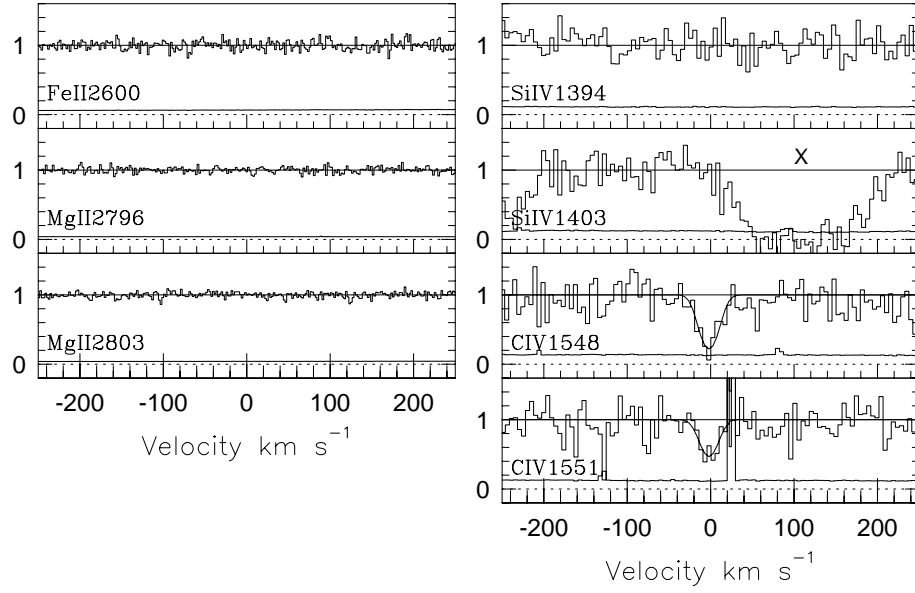


Fig. 15.— Same as the Figure 5, but for the $z_{sys} = 0.7011$ single-cloud high only system in the spectrum of the quasar PG1248+401. Blends are marked with the symbol “X”.

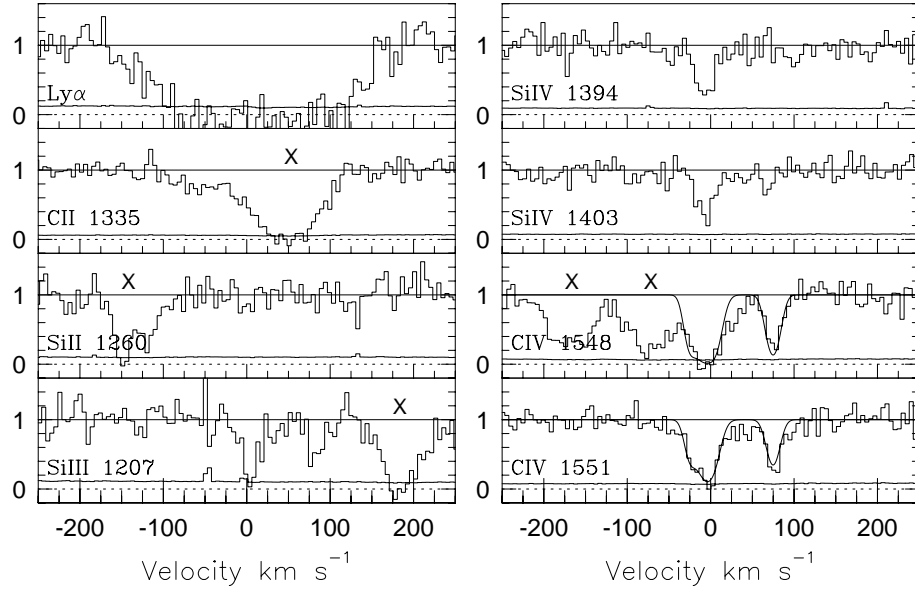


Fig. 16.— Same as Figure 2, but for the system $z = 0.9143$ towards the quasar PG 1630+377. Blends are marked with the symbol “X”.

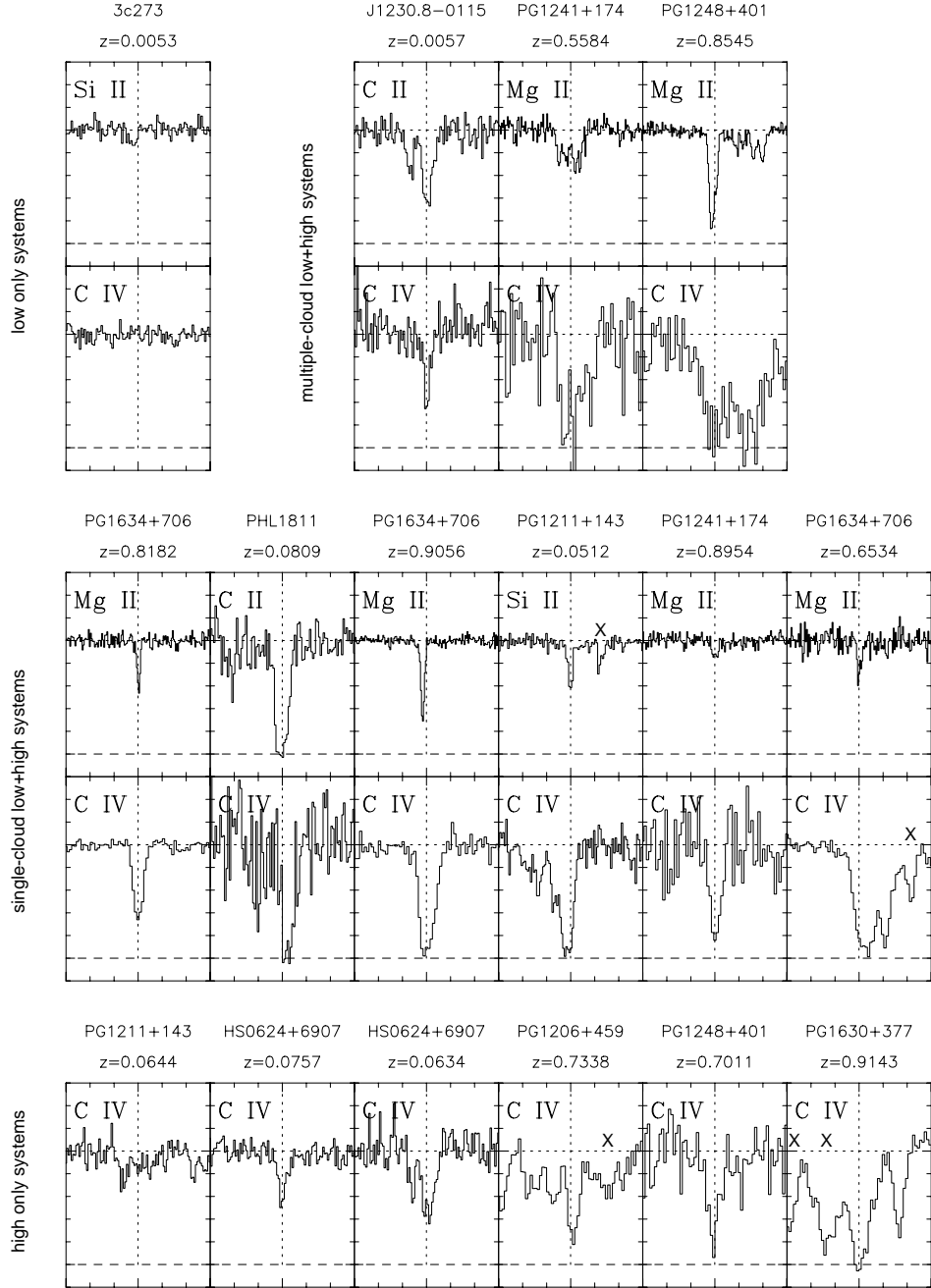


Fig. 17.— The comparison of the kinematic profiles of CIV between the different classes of systems. The first row shows the low ionization only system in the spectrum of the 3C 273 quasar, and the multiple-cloud low + high absorption systems. The low ionization transition with the highest quality data and the CIV λ 1548 transition were used in this illustration. Full system plots appear in Figures 1–16. The second row presents the systems with single-cloud low + high absorption, and the third row shows the CIV λ 1548 profiles for high only systems. The “X” marks indicate blends.

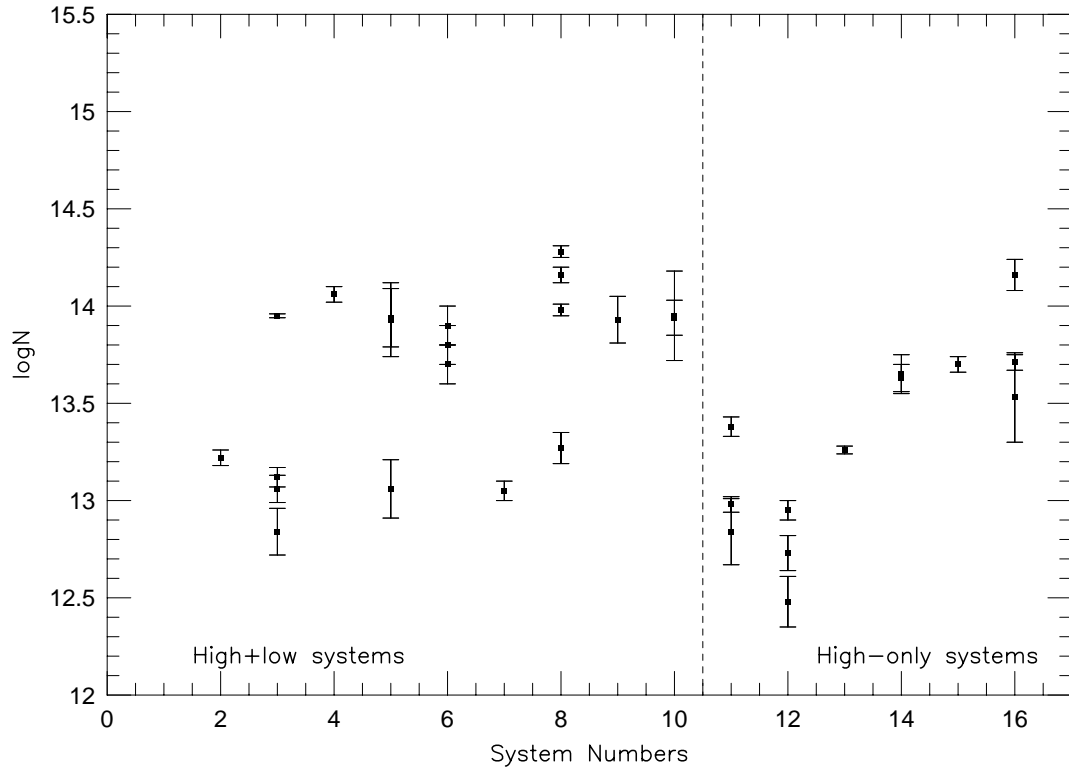


Fig. 18.— The C IV column densities for the individual Voigt profile components in each system. Systems are identified by number in Table 4. The comparison between the C IV in low + high and high only systems shows that high only systems tend to have component C IV column densities less than those of low + high ionization systems.

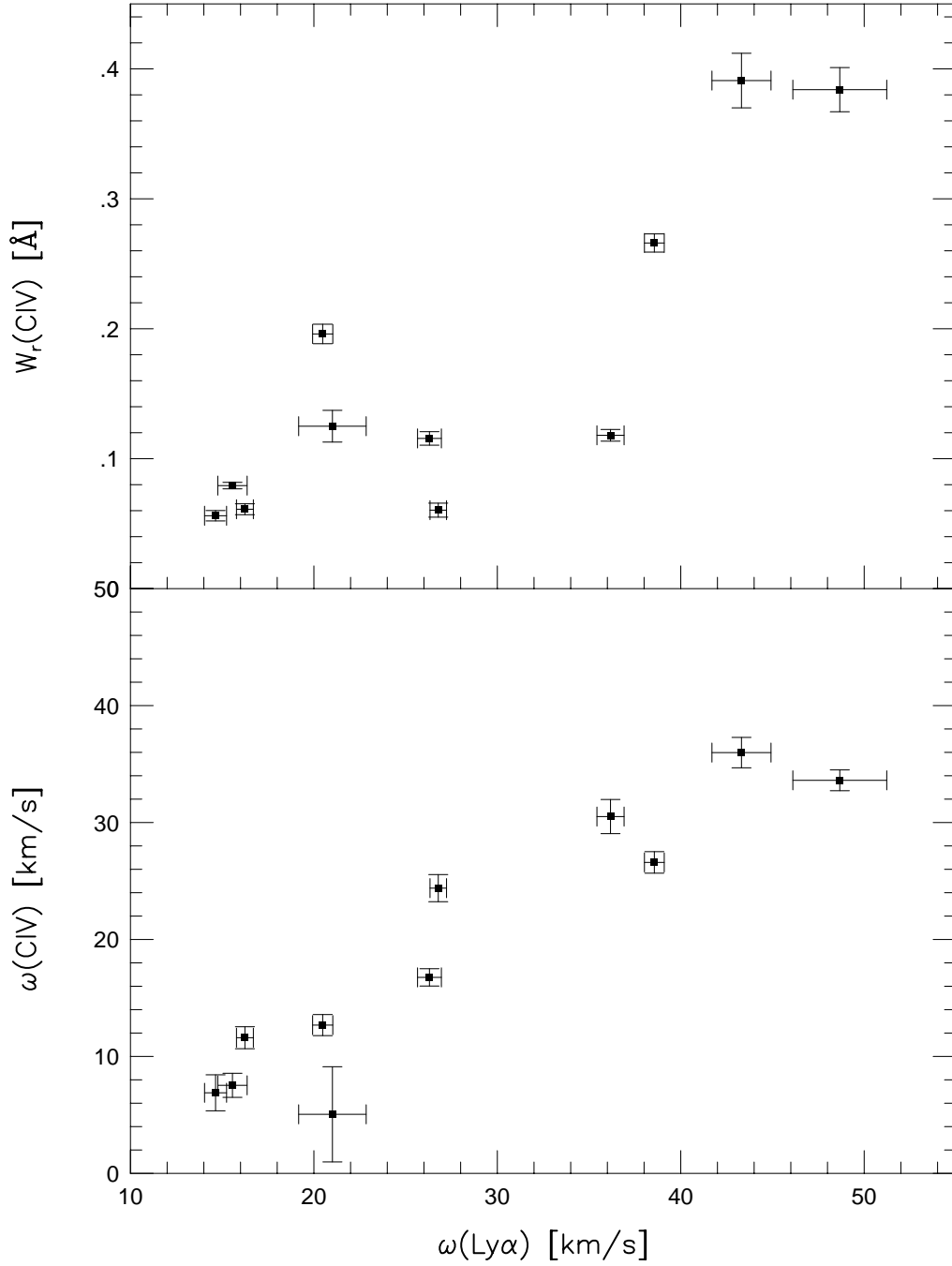


Fig. 19.— Top Panel— Rest frame equivalent width of C IV, $W_r(1548)$, versus kinematic spread of Ly α , $\omega(\text{Ly}\alpha)$. Bottom Panel— Kinematic spread of C IV, $\omega(\text{CIV})$, versus kinematic spread of Ly α , $\omega(\text{Ly}\alpha)$. This higher degree of correlation between $\omega(\text{CIV})$ and $\omega(\text{Ly}\alpha)$ implies that the kinematics of the C IV absorbing gas is a significant factor in determining the strength of the Ly α absorption.

Table 1. *STIS*/HST E140M Grating Data

QSO ID	z_{QSO}	S/N [†] 1216 Å	S/N [†] 1335 Å	S/N [†] 1548 Å	PI	Proposal ID
PKS 0405-123	0.534	4.5	6.4	14.8	Heap	7576
PG 0953+415	0.239	5.9	8.3	5.8	Savage	7747
PG 1116+215	0.177	9.9	10.9	8.8	Sembach/Jenkins	8097/8165
3C 273	0.158	16.3	24.4	18.6	Heap	8017
RX J1230.8+0115	0.117	5.4	9.5	6.3	Rauch	7737
PG 1259+593	0.478	7.0	9.0	5.8	Tripp	8695
PKS 1302-102	0.278	5.2	8.2	8.1	Lemoine	8306
3C 351.0	0.371	5.0	9.2	6.5	Jenkins	8015
H 1821+643	0.297	8.1	19.4	11.5	Jenkins	8165
PKS 2155-304	0.116	13.2	15.9	14.1	Shull	8125
PG 1211+143	0.081	12.5	24.8	12.1	Shull	8571
HS 0624+6907	0.370	5.0	8.8	7.1	Tripp	9184
3C 249.1	0.311	5.6	8.4	5.2	Tripp	4939
PG 1444+407	0.267	4.1	6.8	7.9	Tripp	9184
HE 0226-4110	0.495	5.6	7.7	7.9	Tripp	9184
PHL 1811	0.190	6.4	9.1	7.1	Jenkins	9418
PKS 0312-77	0.223	4.5	6.3	4.2	Kobulnicky	8312
TON S210	0.116	4.0	9.2	5.0	Sembach	9415
PG 1216+069	0.331	4.2	7.2	4.6	Tripp	9184
TON 0028	0.330	4.4	7.0	4.2	Tripp	9184

Note. — † S/N per pixel

Table 2. *STIS*/HST E230M Grating Data

QSO ID	z_{QSO}	S/N [†] 2382 Å	S/N [†] 2796 Å	PI	Proposal ID
PG 0117+210	1.491	8.5	14.2	Jannuzi	8673
PKS 0232-04	1.450	6.1	8.7	Jannuzi	8673
PKS 0312-77	0.223	3.1	5.4	Kobulnicky	8651
PKS 0454-220	0.534	Churchill	8672
HE 0515-4414	1.713	8.1	22.0	Reimers	8288
HS 0747+4259	1.900	4.5	10.1	Reimers	9040
HS 0810+2554	1.500	3.4	5.7	Reimers	9040
PG 1116+215	0.117	10.1	15.1	Sembach	8097
PG 1206+459	1.160	8.4	15.4	Churchill	8672
PG 1241+176	1.273	5.2	20.0	Churchill	8672
PG 1248+401	1.030	8.1	9.6	Churchill	8672
CSO 873	1.022	8.0	10.4	Churchill	8672
PG 1630+377	1.466	8.7	14.8	Jannuzi	8673
PG 1634+706	1.334	19.8	28.5	Jannuzi/Burles	8312/7292
PG 1718+481	1.083	15.9	...	Burles	7292

Note. — † S/N per pixel

Table 3. Restframe Equivalent Widths of Selected Transitions

#	QSO ID	z_{system}	$\text{Ly}\alpha$	MgII	SiII	CII	CIV	SiIV
Low Only Systems								
1	3c 273	0.0053	0.419±0.009	0.019±0.003	< 0.0053	...
Low + High Systems								
2	RX J1230.8+0115	0.0057	0.615±0.006	...	0.103±0.008	0.105±0.005	0.056±0.004	0.078±0.005
3	PG 1211+143	0.0512	1.230±0.005	...	0.048±0.003	0.157±0.003	0.266±0.007	0.083±0.004
4	PHL 1811	0.0809	0.898±0.006	...	0.158±0.007	0.164±0.005	0.118±0.005	0.119±0.002
5	PG 1241+176	0.5584	...	0.132±0.006	0.263±0.020	...
6	PG 1634+706	0.6534	0.665±0.032	0.032±0.005	0.0207±0.008	0.045±0.006	0.384±0.017	0.123±0.008
7	PG 1634+706	0.8181	0.216±0.010	0.036±0.001	0.020±0.004	0.017±0.002	0.079±0.003	0.019±0.003
8	PG 1248+401	0.8545	...	0.246±0.006	0.175±0.040	0.349±0.047	0.873±0.024	...
9	PG 1241+176	0.8954	0.547±0.027	0.019±0.002	0.038±0.007	< 0.021	0.125±0.012	0.047±0.006
10	PG 1634+706	0.9055	0.314±0.005	0.073±0.001	0.055±0.004	0.062±0.003	0.196±0.008	...
High Only Systems								
11	HS 0624+6907	0.0635	0.582±0.022	...	< 0.006	< 0.002	0.116±0.005	...
12	PG 1211+143	0.0644	0.590±0.012	...	< 0.002	< 0.005	0.060±0.006	< 0.013
13	HS 0624+6907	0.0757	0.308±0.007	...	< 0.005	< 0.012	0.061±0.004	0.048±0.005
14	PG 1206+459	0.7338	< 0.011	~ 0.25 †	< 0.021
15	PG 1248+401	0.7011	...	< 0.012	0.114±0.009	...
16	PG 1630+377	0.9143	1.119±0.019	...	0.013±0.0096*	...	0.391±0.021	...

Note. — * 3 σ level detection

† from the measurement of CIV λ 1550, due to the heavy blend in CIV λ 1548

Table 4. Voigt Profile Fits of C IV $\lambda\lambda 1548, 1550$

#	QSO ID	z_{sys}	LogN [cm^{-2}]	ΔLogN [cm^{-2}]	b [km s^{-1}]	Δb [km s^{-1}]	v [km s^{-1}]
Low + High Systems							
2	RX J1230.8+0115	0.0057	13.22	0.04	6.87	0.91	0
3	PG 1211+143	0.0512	12.84	0.12	12.23	4.27	-89
			13.06	0.07	9.56	1.76	-65
			13.12	0.05	6.84	1.03	-36
			13.95	0.01	13.49	0.49	-8
4	PHL 1811	0.0809	14.06	0.04	11.24	0.76	0
5	PG 1241+174	0.5584	13.93	0.19	7.97	2.32	-10
			13.94	0.15	15.09	5.07	1
			13.06	0.15	7.09	3.6	25
6	PG 1634+706	0.6534	~ 13.7		~ 13		-3
			~ 13.9		~ 9		24
			~ 13.8		~ 14		54
7	PG 1634+706	0.8181	13.05	0.05	6.60	1.80	0
8	PG 1248+401	0.8545	14.16	0.04	20.19	4.58	-2
			14.28	0.03	38.86	3.03	70
			13.27	0.08	14.54	3.55	153
			13.98	0.03	26.59	1.74	221
9	PG 1241+174	0.8954	13.93	0.12	7.73	1.07	0
10	PG 1634+706	0.9056	13.95	0.23	5.50	1.80	-2
			13.94	0.09	13.90	1.30	15
High Only Systems							
11	HS 0624+6907	0.0634	12.98	0.04	7.16	1.11	-30
			12.84	0.17	1.79	2.04	-6
			13.38	0.05	12.99	1.55	7
12	PG 1211+143	0.0644	12.95	0.05	10.65	1.58	-23
			12.48	0.13	6.23	3.02	5
			12.73	0.09	10.45	3.00	29
13	HS 0624+6907	0.0757	13.26	0.02	15.06	0.91	0
14	PG 1206+459	0.7338	13.63	0.07	39.69	7.73	-17 *
			13.65	6.99	1.62	9.10	9 *
15	PG 1248+401	0.7011	13.70	0.04	13.26	1.45	0
16	PG 1630+377	0.9143	13.53	0.23	6.59	3.44	-25 *
			14.16	0.08	12.52	2.17	-4 *
			13.71	0.04	8.42	0.70	75

Note. — *Based on fit to C IV $\lambda 1550$ line since there were blends with C IV $\lambda 1548$